

# A low-rank semiparametric Bayesian spatial model for estimating extreme Red Sea surface temperature hotspots

Arnab Hazra<sup>1</sup> and Raphaël Huser<sup>1</sup>

April 22, 2022

## Abstract

In this work, we focus on estimating sea surface temperature (SST) hotspots, i.e., high threshold exceedance regions, for the Red Sea, a vital region of endangered coral reefs. We analyze satellite-derived high-dimensional SST data comprising daily measurements at 16703 grid cells across the Red Sea over the period 1985–2015. We propose a semiparametric Bayesian spatial mixed-effects linear model with a flexible mean structure to capture the spatially-varying trend and seasonality, while the residual spatial variability is modeled through a Dirichlet process mixture (DPM) of low-rank spatial Student- $t$  processes (LTPs). By specifying cluster-specific parameters for each LTP mixture component, the bulk of the SST residuals influence tail inference and hotspot estimation only moderately. Our proposed model has a nonstationary mean, covariance and tail dependence, and posterior inference can be drawn efficiently through Gibbs sampling. In our application, we show that the proposed method outperforms some parametric and semiparametric alternatives. Moreover, we show how hotspots can be identified and we estimate the extreme SST hotspots for the whole Red Sea, projected for the year 2100. The estimated 95% credible region for joint high threshold exceedances include large areas covering major coral reefs in the southern Red Sea.

**Keywords:** Coral bleaching; Dirichlet process mixture model; Extreme event; Low-rank model; Nonstationary mean, covariance and tail dependence; Sea surface temperature data; Student's  $t$  process.

---

<sup>1</sup>Computer, Electrical and Mathematical Sciences and Engineering (CEMSE) Division, King Abdullah University of Science and Technology (KAUST), Thuwal 23955-6900, Saudi Arabia.  
E-mails: arnab.hazra@kaust.edu.sa; raphael.huser@kaust.edu.sa

# 1 Introduction

Sea surface temperature (SST) has an immense impact on marine life and ecosystems, and an increasing trend of SST over the last few decades has affected numerous species including corals (Lewandowska et al., 2014). Coral bleaching is the loss of color in corals due to stress-induced expulsion of unicellular algae (zooxanthellae, for example) living within coral tissues. High SST along with high incident radiation are the primary causes of coral bleaching and mortality (Reaser et al., 2000; Krishnan et al., 2011). In spite of being a region of high biodiversity, the coral reefs of the Red Sea have been studied less than those of the Indian Ocean and the Pacific Ocean (Berumen et al., 2013). Hence, the identification of the regions within the Red Sea where SST may exceed high thresholds over a prolonged period of time is a vital concern and this motivates a proper statistical analysis of extreme hotspots from a high resolution spatiotemporal SST dataset. Operational Sea Surface Temperature and Sea Ice Analysis (OSTIA) produces satellite-derived daily SST data at  $0.05^\circ \times 0.05^\circ$  resolution (Donlon et al., 2012). Over the whole Red Sea, daily SST data are available at 16703 grid cells between 1985–2015 and we consider these data for estimating the extreme hotspots.

The most common model in spatial geostatistics is the Gaussian process (GP) due to its appealing theoretical and computational properties (Gelfand and Schliep, 2016). However, fitting an ordinary GP model involves computing the determinant and the inverse of the spatial covariance matrix, which is excessively prohibitive in dimensions as high as the Red Sea SST data (here, available at 16703 grid cells). A variety of methods have been proposed to tackle this problem. These include approaches based on kernel convolutions (Higdon, 2002), low-rank methods using basis functions (Wikle and Cressie, 1999), the predictive process (Banerjee et al., 2008), approximations of the likelihood in the spectral domain (Stein, 1999; Fuentes, 2007) or by a product of appropriate conditional distributions (Vecchia, 1988; Stein et al., 2004), covariance tapering (Furrer et al., 2006; Anderes et al., 2013) and Markov random fields (Rue and Held, 2005; Rue et al., 2009). Irrespective of being an ordinary GP

or a low-rank GP (LGP) model, the marginal normal density functions are thin-tailed and hence they can heavily underestimate the probabilities of extreme events. Additionally, the tails of multivariate normal distributions lead to independent extremes except in the trivial case of perfect dependence which can result in disastrous underestimation of the simultaneous occurrence probabilities of extreme events (Davison et al., 2013). Hence, both GPs and LGPs are criticized when the main interest is in the tail behavior. Relaxing the parametric GP assumption, Gelfand et al. (2005) propose a flexible nonparametric Bayesian model based on a Dirichlet process mixture (DPM) of spatial GPs in the context of geostatistical analysis; however, Hazra et al. (2018) showed that the tails of the joint distributions for a finite mixture of GPs also lead to independent extremes. While there are more flexible nonparametric spatial models available in the geostatistics literature (see, e.g., Duan et al., 2007), they are not computationally suitable for large spatial datasets.

While GPs and related processes are typically used to describe the bulk behavior, models stemming from extreme-value theory are designed to accurately describe the tail behavior. The classical modeling of spatial extremes usually relies on site-wise block-maxima or peaks over some high threshold (Smith, 1990; Davison et al., 2012, 2019; Davison and Huser, 2015). They can be divided into three main categories: (asymptotic) max-stable and Pareto processes (Smith, 1990; Padoan et al., 2010; Davison et al., 2012; Reich and Shaby, 2012; Opitz, 2013; Thibaud and Opitz, 2015; de Fondeville and Davison, 2018), latent variable models (Sang and Gelfand, 2009, 2010; Cooley and Sain, 2010; Opitz et al., 2018) and sub-asymptotic models (Huser et al., 2017; Morris et al., 2017; Hazra et al., 2019; Huser and Wadsworth, 2019). Max-stable and Pareto processes are asymptotically justified models for spatial extremes but likelihood computations are usually challenging even for low or moderate spatial dimensions (see, e.g., Castruccio et al., 2016; Huser et al., 2019). An exception is the max-stable model of Reich and Shaby (2012), which is computationally tractable for higher spatial dimensions; see also Bopp et al. (2019a). However, this model is constructed from

deterministic kernels and is generally overly smooth in practice. Analogously, [de Fondeville and Davison \(2018\)](#) show how Pareto processes can be efficiently fitted to high-dimensional peaks-over-thresholds using proper scoring rules, but their approach is limited to a few thousand sites and cannot easily be accommodated to the Bayesian setting. Alternatively, [Morris et al. \(2017\)](#) propose a Bayesian model for high threshold exceedances based on the spatial skew- $t$  process, which lacks the strong asymptotic characterization of max-stable and Pareto processes but benefits from exceptionally faster computation. Instead of considering only the block-maxima or peaks-over-thresholds as in the above mentioned approaches, [Hazra et al. \(2018\)](#) consider a DPM of spatial skew- $t$  processes where the extremes are selected probabilistically through the Dirichlet process prior; hence, this modeling approach does not require any arbitrary high thresholding but assumes that identically distributed temporal replicates are available. Recently, [Bopp et al. \(2019b\)](#) propose a Bayesian analogue model for projecting flood-inducing precipitation where the intensity of precipitation is modeled using a mixture of Student’s  $t$  processes. However, both of these approaches are applicable only for low spatial dimension and they are not directly applicable for a large spatiotemporal dataset with trend and seasonality, such as our Red Sea SST dataset.

In this paper, we propose a low-rank semiparametric Bayesian spatial mixed-effects linear model, which extends the spatial model of [Hazra et al. \(2018\)](#), to handle large, highly non-stationary spatiotemporal datasets. The mean SST profile is assumed to be comprised of a spatially-varying linear trend and nonlinear seasonality term (modeled using B-splines). Furthermore, for computational tractability with high spatial resolution, we consider a low-rank approximation of the spatially-varying coefficients involved within the trend and seasonality components. We model the variability using a DPM of low-rank spatial Student- $t$  processes (LTPs), abbreviated by LTP-DPM in short. The DPM is constructed using a (truncated) stick-breaking prior ([Sethuraman, 1994](#)). As for the LTP mixture components, we construct them by a scalar product of multivariate normal random effects with orthonormal spatial

basis functions, then multiplied by an inverse-gamma random scaling. The random effects are assumed to be independent and identically distributed (iid) across time points. The final proposed model has nonstationary mean, covariance and tail dependence structure, and under limiting conditions, it spans all possible squared-integrable spatial processes. We draw posterior inference about the model parameters through an efficient Gibbs sampler.

Besides analyzing the SST data, our ultimate goal is to identify regions at risk, where the SST level might exceed a high threshold at some future time. Similar problems arise in a wide range of scientific disciplines, for example, environmental health monitoring (Bolin and Lindgren, 2015), brain imaging (Mejia et al., 2019), astrophysics (Beaky et al., 1992) and climatology (Furrer et al., 2007; French and Sain, 2013). The easiest and most naive approach for estimating exceedance regions (i.e., hotspots) is to perform site-specific exceedance tests at each grid cell separately (see, e.g., Eklundh and Olsson, 2003). However, such a naive approach does not adequately account for multiple testing, and a better approach is to set the joint probability of exceeding a high threshold over the *whole* region equal to some predefined value. In this spirit, a variety of more advanced methods have been proposed for identifying hotspots (Cressie et al., 2005; Craigmile et al., 2006; French and Sain, 2013; Bolin and Lindgren, 2015). In particular, French and Sain (2013) provide a method to construct confidence regions for Gaussian processes that contain the true exceedance regions with some predefined probability. Here, we develop an approach to estimate extreme hotspots by extending the Gaussian-based method of French and Sain (2013) to our highly flexible semiparametric LTP-DPM model, which is better suited for capturing the joint tail behavior.

The paper is organized as follows. In §2, we present the Red Sea SST dataset and some exploratory analysis. Our proposed LTP-DPM model and its properties are discussed in §3. In §4, we discuss Bayesian computational details and the hotspot estimation technique. In §5, we apply the proposed methodology to the Red Sea SST dataset and discuss the results. We conclude with some discussion and perspectives on future research in §6.

## 2 The Red Sea SST dataset and exploratory analysis

The OSTIA project generates satellite-derived daily SST estimates (free of diurnal variability) at an output grid resolution of  $0.05^\circ \times 0.05^\circ$  (about 6 km). This yields 16703 grid cells for the whole Red Sea. The data can be freely obtained from the website [http://ghrsst-pp.metoffice.com/pages/latest\\_analysis/ostia.html](http://ghrsst-pp.metoffice.com/pages/latest_analysis/ostia.html). Figure 1 shows spatial maps of observed SST profiles for three days with high spatially-averaged SST. For all three days, the SST values are lowest near the Gulfs of Aqaba and Suez in the North, and highest in the southern Red Sea near the coast of Eritrea and the southwest of Saudi Arabia.

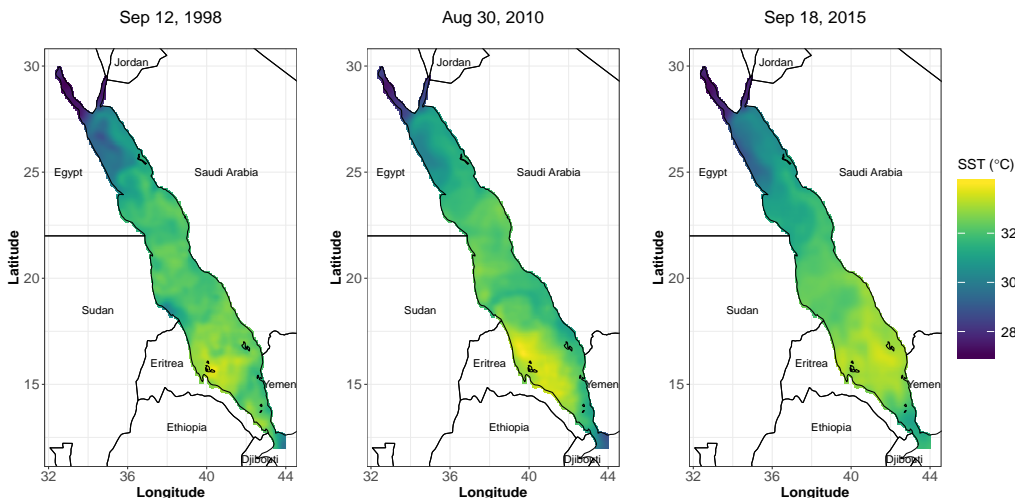


Figure 1: Observed SST profiles across the Red Sea for three extremely hot days: September 12, 1998 (left), August 30, 2010 (middle), and September 18, 2015 (right). All sub-figures are on the same scale.

Some exploratory analysis (not shown) reveals that daily SST data are highly autocorrelated in time, and that the strength of temporal dependence varies strongly over space. Considering the high spatial dimension, it would be statistically and computationally challenging to account for spatially-varying autocorrelation in a flexible way in our model. Therefore, for simplicity, we here analyze temporally-thinned data, keeping only one day per week at each grid cell. Thus, we obtain seven sub-datasets. This reduces the temporal autocorrelation, so that the observations can be safely assumed to be temporally independent within each

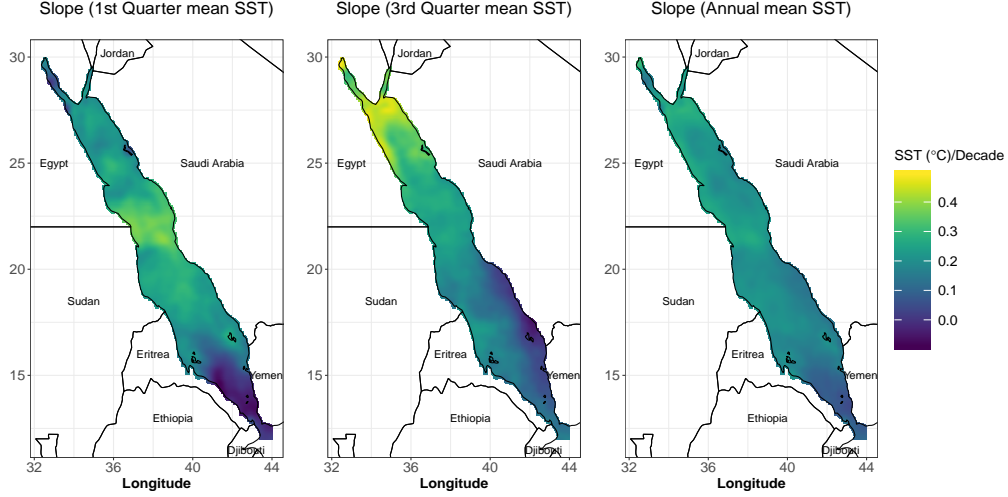


Figure 2: Estimated slopes for site-wise simple linear regression model fits performed on quarterly average SST for the first (left) and the third (middle) quarters and also on annual average SST (right) over the Red Sea. All sub-figures are on the same scale.

sub-dataset, and we obtain 1612 replicates (i.e., one for each week) of the spatial process. The results are observed to be very similar across the sub-datasets. In this paper, we obtain the results separately for each sub-dataset and report the averages. The effectiveness of this approach could be limited for temporal prediction at small lags but considering our main goal is in drawing spatial inference, analyzing temporally-thinned data seems to be reasonable.

Considering the spatially-varying nature of SST across the Red Sea and the long data collection period of 31 years from 1985 to 2015, a period that faced global warming, we first conduct a preliminary site-by-site trend analysis by fitting simple linear regression models to the annual mean SST as well as the quarterly mean SST. The estimated intercept and slope profiles in all three cases vary over space. The mean SST across the Red Sea is lowest during the first quarter and highest during the third quarter. The estimated slope profiles of the first-quarterly, third-quarterly and annual mean SST are displayed in Figure 2. For the first quarterly and annual mean SST, the slopes are the highest near the latitude  $22^{\circ}\text{N}$  and are the lowest near the southern end of the Red Sea between Eritrea and Yemen. However, for the third quarterly mean SST, the highest slopes are observed throughout the coast of Egypt in the northwest, and the lowest values are observed near the southwest of Saudi Arabia. Thus,

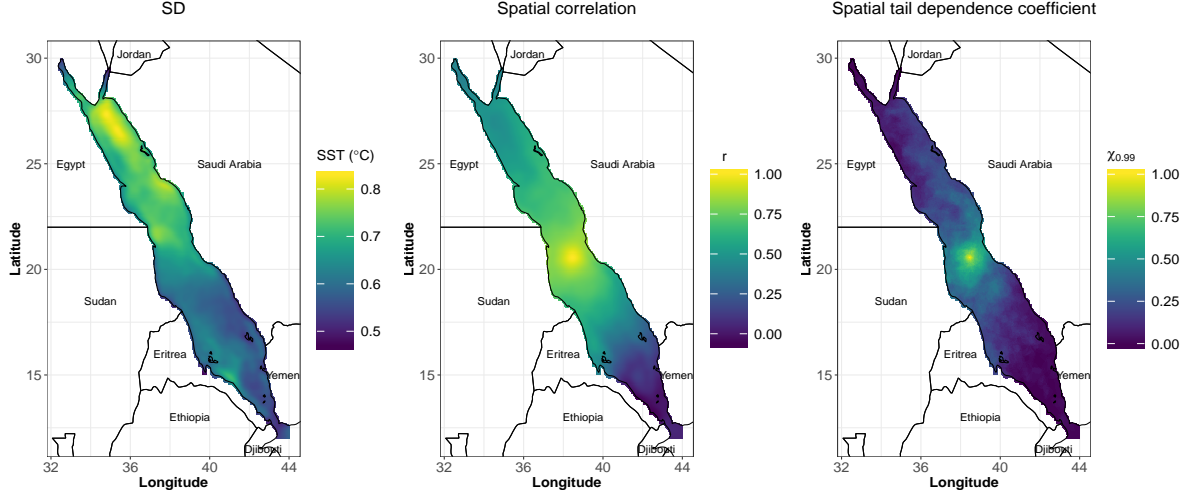


Figure 3: Grid cell-wise SD (left), spatial correlation ( $r$ , middle) and extremal dependence ( $\chi_{0.99}$ , right) profiles corresponding to the grid cell ( $38.48^\circ\text{E}$ ,  $20.62^\circ\text{N}$ ), respectively.

Figure 2 explains the need for spatially-, as well as seasonally- or weekly-varying coefficients for modeling the marginal SST distributions.

We then study the seasonality profile (averaged across years) at various grid cells. Significantly different patterns are observed throughout the Red Sea. The hottest weeks (maximizing the annual weekly average SST) vary mainly between weeks 32 and 35 (above the latitude  $20^\circ\text{N}$ ), and weeks 37 and 42 (below  $20^\circ\text{N}$ ). The observed nonstationarity of SST across weeks explains the need for a flexible modeling of seasonality, e.g., through some linear combination of local basis functions with spatially-varying coefficients.

We then compute the site-wise standard deviations (SDs) of the detrended SST data (obtained by spline smoothing as discussed in Section 3.2). The results are presented in the left panel of Figure 3. Again, there is a highly nonstationary pattern, with high SDs near the northeast region and low SDs near the southeast region. The middle panel of Figure 3 shows the spatial correlation structure with respect to the central grid cell ( $38.48^\circ\text{E}$ ,  $20.62^\circ\text{N}$ ). The correlation values in the northern region are significantly higher than the values in the southern region despite being at the same distance. This suggests that the spatial correlation structure is also highly nonstationary.



To investigate the extremal dependence structure, we compute the empirical tail dependence coefficient with respect to the same grid cell (38.48°E, 20.62°N). The tail dependence coefficient between two random variables  $Y_1$  and  $Y_2$  is defined as  $\chi = \lim_{u \rightarrow 1} \chi_u$ , where

$$\chi_u = \Pr \{Y_1 > F_1^{-1}(u) \mid Y_2 > F_2^{-1}(u)\}, \quad (1)$$

and  $F_1$  and  $F_2$  are the marginal distribution functions of  $Y_1$  and  $Y_2$ , respectively. A nonzero value of  $\chi$  indicates asymptotic dependence while  $\chi = 0$  indicates asymptotic independence. Here, we estimate  $\chi$  with the empirical conditional probability  $\hat{\chi}_u$  with  $u = 0.99$ . The values are reported on the right panel of Figure 3. The observed values are nonzero throughout a major portion of the spatial domain indicating the necessity for a model that can capture nonzero extremal dependence (unlike GPs) at large distances and high thresholds.

Finally, we investigate the bias in estimating high quantiles when fitting normal and Student's  $t$  distributions. High biases observed at many grid cells indicate the need for a more flexible model than the usual parametric alternatives. As mixture models fit low through high quantiles of the distributions more flexibly, a semiparametric model is warranted.

More details on the exploratory analysis are provided in the Supplementary Material. Summarizing, we need a model that allows spatially-varying trend and seasonality components within the mean structure, while the residual variability needs to be modeled through a mixture of spatial processes that allows for extremal dependence. Considering the high dimension, a low-rank approach is necessary to ensure that inference is practically feasible.

## 3 Modeling

### 3.1 General framework

Let  $\mathcal{D}$  denote the spatial domain of the Red Sea. We model the Red Sea SST data as

$$Y_t(\mathbf{s}) = \mu_t(\mathbf{s}) + \varepsilon_t(\mathbf{s}), \quad (2)$$

where  $Y_t(\mathbf{s})$  denotes the observed SST at location  $\mathbf{s} \in \mathcal{D}$  and at time  $t \in \{1, 2, \dots, T = 1612\}$ ,  $\mu_t(\mathbf{s})$  is the mean SST profile and  $\varepsilon_t(\mathbf{s})$  is the corresponding error component.

In §3.2, we first discuss the modeling of the mean term  $\mu_t(\mathbf{s})$ , and in §3.3, we then discuss the modeling of the residual process  $\varepsilon_t(\mathbf{s})$  for  $\mathbf{s} \in \mathcal{D}$  and  $t \in \{1, 2, \dots, T\}$ . In §3.4, we specify the overall Bayesian model, and in §3.5, we describe the model properties.

## 3.2 Mean modeling

By an abuse of notation, we write  $\mu_t(\mathbf{s}) = \mu(t_1, t_2, \mathbf{s})$  where  $t_1 = \lceil t/52 \rceil$  denotes the year corresponding to time  $t$  and  $t_2 = t - 52(t_1 - 1)$  denotes the corresponding week within the  $t_1$ -th year. Here,  $t_1 \in \{1, \dots, T_1 = 31\}$  for 31 years of data and  $t_2 \in \{1, \dots, T_2 = 52\}$  for the 52 weeks within each year. Henceforth, this one-to-one relation between  $t$  and  $(t_1, t_2)$  holds for the rest of the paper. In spite of the data being observed at discrete time points, we model the mean SST profile as a continuous function of  $t_1$  and  $t_2$ .

We assume that  $\mu(t_1, t_2, \mathbf{s})$  is linear in  $t_1$  with  $\mu(t_1, t_2, \mathbf{s}) = \beta_1(t_2, \mathbf{s})x_{t_1,1}^{(0)} + \beta_2(t_2, \mathbf{s})x_{t_1,2}^{(0)}$ , where  $\beta_1(t_2, \mathbf{s})$  and  $\beta_2(t_2, \mathbf{s})$  denote the intercept and slope coefficients that vary over space, as well as for each week of a specific year. Let  $\mathbf{X}_0$  denote the  $(T_1 \times 2)$ -dimensional matrix with  $(t_1, p_0)$ -th entry denoted by  $x_{t_1, p_0}^{(0)}$ ,  $p_0 = 1, 2$ . We consider standardized covariates,  $x_{t_1,1}^{(0)} = 1/\sqrt{T_1}$  and  $x_{t_1,2}^{(0)} = \{t_1 - (1 + T_1)/2\}/\sqrt{\sum_{t_1^*=1}^{T_1} \{t_1^* - (1 + T_1)/2\}^2}$ , which ensures that  $\mathbf{X}_0$  is an orthonormal matrix. This is important from a computational perspective.

We then further model the regression coefficients  $\beta_{p_0}(t_2, \mathbf{s})$ ,  $p_0 = 1, 2$ , as  $\beta_{p_0}(t_2, \mathbf{s}) = \sum_{p_1=1}^{P_{\mathcal{T}}} \beta_{p_0, p_1}(\mathbf{s})x_{t_2, p_1}^{(1)}$ , where  $x_{t_2, p_1}^{(1)}$ ,  $p_1 = 1, \dots, P_{\mathcal{T}}$ , are cubic B-splines defined over the continuous interval  $[1, T_2]$  with equidistant knots and evaluated at  $t_2$ . Considering one B-spline per month, we have  $P_{\mathcal{T}} = 12$ . For convenience, here we assume that the B-spline basis functions are the same for  $p_0 = 1, 2$ , though other choices are also possible. We denote the corresponding  $(T_2 \times P_{\mathcal{T}})$ -dimensional design matrix by  $\mathbf{X}_1$ , with  $(t_2, p_1)$ -th entry  $x_{t_2, p_1}^{(1)}$ .

Finally, let the grid cells within  $\mathcal{D}$  be denoted by  $\mathbf{s}_1, \dots, \mathbf{s}_N$ . In order to reduce the computational burden due to the high spatial dimension  $N = 16703$ , we consider a low-rank approximation of the spatially-varying coefficients by specifying  $\beta_{p_0, p_1}(\mathbf{s}_n) = \sum_{p_2=1}^{P_{\mathcal{S}}} \beta_{p_0, p_1, p_2} x_{n, p_2}^{(2)}$

where  $x_{n,p_2}^{(2)}$  are suitable spatial basis functions. While other choices are also possible, we consider a tensor product of cubic B-splines defined over a rectangular surface covering  $\mathcal{D}$ . Taking the elongated geometry of the Red Sea into account, we place 30 equidistant B-splines along the northwest–southeast direction and 10 equidistant B-splines along the west–east direction. Out of these 300 B-splines, we only keep the  $P_S = 189$  of them that represent more than 99% of the total weight over  $\mathbf{s}_1, \dots, \mathbf{s}_N$ . The knots are well spread across all the Red Sea and hence the splines are able to capture local characteristics well. We denote the corresponding  $(N \times P_S)$ -dimensional design matrix by  $\mathbf{X}_2$ , with  $(n, p_2)$ -th entry  $x_{n,p_2}^{(2)}$ .

In summary, we model the mean SST at spatial location  $\mathbf{s}_n$  and time point  $t$  as

$$\mu_t(\mathbf{s}_n) = \sum_{p_0=1}^2 \sum_{p_1=1}^{P_T} \sum_{p_2=1}^{P_S} \beta_{p_0,p_1,p_2} x_{t_1,p_0}^{(0)} x_{t_2,p_1}^{(1)} x_{n,p_2}^{(2)}. \quad (3)$$

Let the spatial mean vector at time  $t$  be  $\boldsymbol{\mu}_t = [\mu_t(\mathbf{s}_1), \dots, \mu_t(\mathbf{s}_N)]'$ , and combining all time points, let  $\boldsymbol{\mu} = [\boldsymbol{\mu}'_1, \dots, \boldsymbol{\mu}'_T]'$ . Grouping the regression coefficients, let  $\boldsymbol{\beta}_{p_0,p_1} = [\beta_{p_0,p_1,1}, \dots, \beta_{p_0,p_1,P_S}]'$  and  $\boldsymbol{\beta}_{p_0} = [\boldsymbol{\beta}'_{p_0,1}, \dots, \boldsymbol{\beta}'_{p_0,P_T}]'$ . Denoting the two columns of  $\mathbf{X}_0$  by  $\mathbf{X}_{0;1}$  and  $\mathbf{X}_{0;2}$ , respectively, we can write  $\boldsymbol{\mu}$  in vectorial form as  $\boldsymbol{\mu} = [\mathbf{X}_{0;1} \otimes \mathbf{X}_1 \otimes \mathbf{X}_2] \boldsymbol{\beta}_1 + [\mathbf{X}_{0;2} \otimes \mathbf{X}_1 \otimes \mathbf{X}_2] \boldsymbol{\beta}_2$ , where  $\otimes$  denotes the Kronecker product between two matrices.

### 3.3 Spatial dependence modeling

We now discuss the modeling of the residual process  $\varepsilon_t(\mathbf{s})$ . We here assume that the  $\varepsilon_t(\mathbf{s})$ 's are iid across time, with zero mean, and we write  $\varepsilon(\mathbf{s})$  for a generic copy of  $\varepsilon_t(\mathbf{s})$ . Our semiparametric Bayesian model for the spatial residual processes  $\varepsilon_t(\cdot)$  is based on a Dirichlet process mixture (DPM) of parametric low-rank Student- $t$  processes (LTPs). We first describe the construction of LTPs, and then discuss the modeling based on mixtures.

**Low-rank Student- $t$  process (LTP).** LTPs are richer than LGPs as they have heavier marginal and joint tails, and they can capture spatial extremal dependence contrary to

Gaussian processes. At a spatial location  $\mathbf{s}$ , we model a realization from a LTP as

$$\varepsilon(\mathbf{s}) = \sigma \{ \mathbf{h}'(\mathbf{s}) \mathbf{Z} + \eta(\mathbf{s}) \}, \quad \mathbf{s} \in \mathcal{D}, \quad (4)$$

where  $\mathbf{h}(\mathbf{s})$  denotes the vector of length  $L$  comprised of some spatial basis functions evaluated at  $\mathbf{s}$ . The random effects are specified as  $\mathbf{Z} \sim \text{Normal}_L(\mathbf{0}, \Phi)$ ,  $\sigma^2 \sim \text{Inverse-Gamma}(\frac{a}{2}, \frac{a}{2} - 1)$ , for some positive definite matrix  $\Phi$  and  $a > 2$ , and  $\eta(\cdot)$  denotes a spatial white noise process (i.e., nugget effect) such that  $\eta(\mathbf{s}) \stackrel{iid}{\sim} \text{Normal}(0, \tau^2)$ .

For the  $N$  spatial grid cells  $\mathbf{s}_1, \dots, \mathbf{s}_N$ , let  $\boldsymbol{\varepsilon} = [\varepsilon(\mathbf{s}_1), \dots, \varepsilon(\mathbf{s}_N)]'$  be the vector of observed values from the process  $\varepsilon(\cdot)$ . Moreover, let  $\mathbf{H}$  be the  $(N \times L)$ -dimensional matrix, whose columns are the different spatial basis functions evaluated at  $\mathbf{s}_1, \dots, \mathbf{s}_N$ . After marginalization over the random effects  $\mathbf{Z}$  and  $\sigma^2$ , the joint distribution of  $\boldsymbol{\varepsilon}$  is

$$\boldsymbol{\varepsilon} \sim T_a(\mathbf{0}_N, \frac{a-2}{a} \{ \mathbf{H} \Phi \mathbf{H}' + \tau^2 \mathbf{I}_N \}), \quad (5)$$

where  $T_{\tilde{a}}(\tilde{\boldsymbol{\mu}}, \tilde{\boldsymbol{\Sigma}})$  denotes the multivariate Student's  $t$  distribution with location vector  $\tilde{\boldsymbol{\mu}}$ , dispersion matrix  $\tilde{\boldsymbol{\Sigma}}$  and degrees of freedom  $\tilde{a}$ ,  $\mathbf{I}_N$  is the  $N$ -by- $N$  identity matrix, and  $\mathbf{0}_N$  is the zero vector of length  $N$ . In case (temporal) replications are available from the spatial process  $\varepsilon(\cdot)$ , the spatial covariance matrix of  $\boldsymbol{\varepsilon}$  (which exists since  $a > 2$ ) can be estimated using the sample covariance matrix  $\hat{\boldsymbol{\Sigma}} = \widehat{\text{Cov}}(\boldsymbol{\varepsilon})$ . Here, we consider spatial basis functions to be the  $L \ll N$  eigenvectors of  $\hat{\boldsymbol{\Sigma}}$  with the largest corresponding eigenvalues. In other words, the matrix  $\mathbf{H}$  is comprised of empirical orthogonal functions (EOFs). Specifically, let  $\boldsymbol{\Delta}$  be the diagonal matrix with the  $L$  largest eigenvalues of  $\hat{\boldsymbol{\Sigma}}$ , and  $\mathbf{H}$  be the matrix with the column vectors equal to the corresponding eigenvectors. Then, we have the approximation,  $\hat{\boldsymbol{\Sigma}} \approx \mathbf{H} \boldsymbol{\Delta} \mathbf{H}'$ . Other choices of basis functions  $\mathbf{h}(\mathbf{s})$  are also possible (even in case replications are unavailable); a detailed discussion regarding the choices of  $\mathbf{h}(\mathbf{s})$  is provided in [Wikle \(2010\)](#). While  $\Phi = \boldsymbol{\Delta}$  could be assumed, we consider instead  $\Phi$  to be unknown and use an informative prior on  $\Phi$  with prior mean equal to  $\boldsymbol{\Delta}$ . The nugget component  $\boldsymbol{\eta} = [\eta(\mathbf{s}_1), \dots, \eta(\mathbf{s}_N)]'$  is important for  $\text{Cov}(\boldsymbol{\varepsilon})$  to be full-rank and also  $\tau^2$  is expected to be small. The specific

parametrization of  $\sigma^2$  ensures that  $\text{Cov}(\boldsymbol{\varepsilon}) = \mathbf{H}\boldsymbol{\Phi}\mathbf{H}' + \tau^2\mathbf{I}_N$ , so plugging the prior mean of  $\boldsymbol{\Phi}$ , we get the approximation  $\text{Cov}(\boldsymbol{\varepsilon}) \approx \mathbf{H}\boldsymbol{\Delta}\mathbf{H}' + \tau^2\mathbf{I}_N \approx \widehat{\boldsymbol{\Sigma}}$ . Hence, we construct a zero-mean LTP, where the covariance structure resembles the sample covariance.

**Dirichlet process mixture (DPM) of LTPs.** In case we do not have any (temporal) replicates of the process  $\varepsilon(\cdot)$ , parametric assumptions are required (though  $\widehat{\boldsymbol{\Sigma}}$ —and hence  $\mathbf{H}$ —are not available and other choice of basis functions is required). However, for the Red Sea data, independent temporal replications of the anomalies,  $\varepsilon_t(\mathbf{s})$ ,  $t = 1, \dots, T$ , are available and we can thus estimate the underlying spatial process semiparametrically.

Considering that our focus mainly lies in inferences from the tail, here we extend the construction (4) by modeling the residuals using a DPM in the same vein as Hazra et al. (2018), where the characteristics of the bulk and the tail of the anomaly process are described by different mixture components with component-specific parameters. Thus, our approach can automatically and probabilistically cluster observations into weeks characterized by “extreme conditions” or weeks characterized by “normal conditions”, without any artificial and subjective thresholding. Thus, tail inference is expected to be minimally influenced by observations from the bulk, while providing a reasonable fit on the entire probability range.

Now, we assume that for all  $t$ ,  $\boldsymbol{\varepsilon}_t = [\varepsilon_t(\mathbf{s}_1), \dots, \varepsilon_t(\mathbf{s}_N)]'$  are *iid*  $N$ -dimensional realizations from a LTP-DPM model with  $K$  mixture components for some natural number  $K$ . The corresponding multivariate density function is

$$f_{\text{DPM}}(\boldsymbol{\varepsilon}) = \sum_{k=1}^K \pi_k f_T(\boldsymbol{\varepsilon}; \boldsymbol{\Theta}_k), \quad (6)$$

where  $\pi_k > 0$  are the mixture probabilities with  $\sum_{k=1}^K \pi_k = 1$ ,  $\boldsymbol{\Theta}_k$  denotes the set of parameters of the  $k$ -th LTP component, and  $f_T(\cdot)$  denotes the density of a  $N$ -dimensional realization from the LTP as described in (5). When  $K = \infty$ , the model becomes fully nonparametric.

The main advantage of the LTP-DPM model lies in its hierarchical Bayesian model representation. The model can be rewritten as a clustering model, where, conditional on

the random cluster label  $g_t$  with mass function  $\Pr(g_t = k) = \pi_k$ ,  $k \in \{1, \dots, K\}$ , we have  $\varepsilon_t \sim f_T(\cdot \mid \Theta_{g_t})$ . Thus, our LTP-DPM model assumes that weeks with similar residuals can be clustered together, their distribution being described by the same LTP. Treating the cluster labels  $g_t$  as unknown, the model accounts for uncertainty in cluster allocation.

We assign a truncated stick-breaking prior distribution (Sethuraman, 1994) on the mixture probabilities,  $\pi_k$ ,  $k \in \{1, \dots, K\}$ . Precisely, we have the following constructive representation:  $\pi_1 = V_1 \sim \text{Beta}(1, \delta)$  for some Dirichlet process concentration parameter  $\delta > 0$ , and subsequently,  $\pi_k = (1 - \sum_{i=1}^{k-1} \pi_i) V_k$  for  $k = 1, \dots, K-1$  with  $V_k \stackrel{\text{iid}}{\sim} \text{Beta}(1, \delta)$ . As we consider  $K$  to be finite, we set  $V_K = 1$  so that  $\sum_{k=1}^K \pi_k = 1$ . In our MCMC implementation, we exploit the one-to-one correspondence between the  $\pi_k$ 's and the  $V_k$ 's, by iteratively updating the latter to estimate the former. We write  $\boldsymbol{\pi} = [\pi_1, \dots, \pi_K]' \sim \text{Stick-Breaking}(\delta)$ .

### 3.4 Overall model

Considering two types of spatial basis functions within  $\mu_t(\mathbf{s})$  and  $\varepsilon_t(\mathbf{s})$  leads to collinearity issues between fixed and random effects. To fix this issue, we divide the matrix  $\mathbf{X}_2$  from §3.2 into two parts based on its projection onto the column space the matrix  $\mathbf{H}$  from §3.3. The projection matrix is  $\mathbf{P}_H = \mathbf{H}(\mathbf{H}'\mathbf{H})^{-1}\mathbf{H}' = \mathbf{H}\mathbf{H}'$ , as  $\mathbf{H}$  is an orthonormal matrix. We have  $\mathbf{X}_2 = \mathbf{X}_{2;1} + \mathbf{X}_{2;2}$  where  $\mathbf{X}_{2;1} = \mathbf{P}_H\mathbf{X}_2$ , and  $\mathbf{X}_{2;2} = (\mathbf{I}_N - \mathbf{P}_H)\mathbf{X}_2$ , and then rewrite  $\boldsymbol{\mu} = \sum_{i=1}^2 \sum_{j=1}^2 (\mathbf{X}_{0;i} \otimes \mathbf{X}_1 \otimes \mathbf{X}_{2;j}) \boldsymbol{\beta}_{i;j}$  with two separate vectors of coefficients corresponding to  $\mathbf{X}_{2;1}$  and  $\mathbf{X}_{2;2}$  for each of the intercept-related and slope-related terms. For a specific grid cell  $\mathbf{s}_n$  and time point  $t$ ,  $\mu_t(\mathbf{s}_n) = \sum_{i=1}^2 \sum_{j=1}^2 x_{t_1}^{(0;i)} \left( \mathbf{x}_{t_2}^{(1)} \otimes \mathbf{x}_n^{(2;j)} \right) \boldsymbol{\beta}_{i;j}$ , where  $x_{t_1}^{(0;i)}$  is the  $t_1$ -th entry of  $\mathbf{X}_{0;i}$ ,  $\mathbf{x}_{t_2}^{(1)}$  is the  $t_2$ -th row of  $\mathbf{X}_1$ , and  $\mathbf{x}_n^{(2;j)}$  is the  $n$ -th row of  $\mathbf{X}_{2;j}$ .

Overall, our hierarchical model is defined as follows. Given the cluster label  $g_t = k$ ,

$$\begin{aligned} Y_t(\mathbf{s}) &= \mu_t(\mathbf{s}) + \sigma_t \{ \mathbf{h}'(\mathbf{s}) \mathbf{Z}_t + \eta_t(\mathbf{s}) \}, \\ \mathbf{Z}_t &\sim \text{Normal}_L(\mathbf{0}, \Phi_k), \quad \eta_t(\mathbf{s}) \stackrel{\text{iid}}{\sim} \text{Normal}(0, \tau_k^2), \\ \sigma_t^2 &\sim \text{Inverse-Gamma}\left(\frac{a_k}{2}, \frac{a_k}{2} - 1\right), \end{aligned} \tag{7}$$

where  $\mu_t(\mathbf{s})$  is the mean SST profile,  $\mathbf{h}(\mathbf{s})$  is the vector of spatial basis functions as described in Section 3.3, and  $\mathbf{Z}_t$  and  $\sigma_t$  denote independent copies of the corresponding random effects. The set of parameters of the LTP corresponding to time  $t$  is  $\Theta_k = \{\Phi_k, \tau_k^2, a_k\}$ . We treat the cluster-specific parameters  $\Theta_k$  as unknown and put hyperpriors on them. We assume that  $\Theta_k \stackrel{\text{iid}}{\sim} G_{\Theta}$ , with the components of  $\Theta_k$ , i.e.,  $\Phi_k, \tau_k^2$  and  $a_k$  are treated as independent of each other. Our choice of hyperpriors is discussed in §4.1.

### 3.5 Model properties

For Model (7), the conditional mean and covariance structure of  $Y_t(\mathbf{s}_n)$  given the coefficients  $\beta_{i;j}$ , and the cluster-specific parameters  $\Theta_k$  are

$$\begin{aligned} \mathbb{E}\{Y_t(\mathbf{s}_n) \mid \beta_{i;j}, i, j = 1, 2\} &= \mu_t(\mathbf{s}_n) = \sum_{i=1}^2 \sum_{j=1}^2 x_{t_1}^{(0;i)} \left( \mathbf{x}_{t_2}^{(1)} \otimes \mathbf{x}_n^{(2;j)} \right) \beta_{i;j}, \\ \text{Cov}\{Y_t(\mathbf{s}_{n_1}), Y_t(\mathbf{s}_{n_2}) \mid \Theta_k; k = 1, \dots, K\} &= \sum_{k=1}^K \pi_k \left( \mathbf{h}_{n_1} \Phi_k \mathbf{h}_{n_2}' + \tau_k^2 \mathbb{I}_{\{n_1=n_2\}} \right), \end{aligned} \quad (8)$$

where  $\mathbf{h}_n$  denotes the  $n$ -th row of  $\mathbf{H}$  and  $\mathbb{I}_{\{n_1=n_2\}} = 1$  if  $n_1 = n_2$  and zero otherwise.

The mean structure is clearly nonstationary both in space and time, non-linear and includes interaction terms between the spatial and temporal effects. Thus, the model can capture spatially-varying seasonality and trend as well as seasonally-varying trends at each spatial grid cell. Because we specify high-resolution B-spline knot locations both over space and time, our model can capture the local features in the mean behavior reasonably well.

The covariance between the observations at grid cells  $\mathbf{s}_{n_1}$  and  $\mathbf{s}_{n_2}$  is dependent on both  $\mathbf{s}_{n_1}$  and  $\mathbf{s}_{n_2}$  and cannot be reduced to a function of the spatial lag  $\mathbf{s}_{n_1} - \mathbf{s}_{n_2}$ . Hence, the covariance structure is also nonstationary. For the Dirichlet process atoms  $\Phi_k$ ,  $k = 1, \dots, K$ , we consider priors so that  $\mathbb{E}(\Phi_k) = \Delta$ ; recall §3.3. Marginalizing over  $\Phi_k$ , we get  $\text{Cov}\{Y_t(\mathbf{s}_{n_1}), Y_t(\mathbf{s}_{n_2})\} = \mathbf{h}_{n_1} \Delta \mathbf{h}_{n_2}' + \tau^2 \mathbb{I}_{\{n_1=n_2\}}$ , where  $\tau^2 = \sum_{k=1}^K \pi_k \tau_k^2$ . Considering  $\tau^2$  to be small, we get the approximation  $\text{Cov}(\mathbf{Y}_t) \approx \hat{\Sigma}$ , where  $\mathbf{Y}_t = [Y_t(\mathbf{s}_1), \dots, Y_t(\mathbf{s}_N)]'$  and  $\hat{\Sigma}$  is as discussed in §3.3. Thus, the LTP-DPM model is centered around a low-rank Student's  $t$

process, constructed as in §3.3 with mean structure discussed in §3.2.

In case we consider all eigenvectors of  $\widehat{\Sigma}$  in the matrix  $\mathbf{H}$ , i.e.,  $L = N$ , there is no need to consider a nugget term to make sure  $\text{Cov}(\mathbf{Y}_t)$  is full-rank. Considering  $\varepsilon_t(\cdot)$  as an infinite-dimensional spatial process and ignoring the nugget term, for  $L = \infty$ , we can write  $\varepsilon_t(\mathbf{s}) = \sum_{l=1}^{\infty} Z_{lt} h_l(\mathbf{s})$ . For any pair  $l_1$  and  $l_2$  with  $l_1 \neq l_2$ , the vector  $[Z_{l_1 t}, Z_{l_2 t}]'$  follows a DPM of bivariate zero-mean Student's  $t$  distributions which spans any bivariate zero-mean distribution when  $K = \infty$ . Integrating with respect to the priors of  $\Phi_k$ ,  $\text{Cov}(Z_{l_1 t}, Z_{l_2 t}) = 0$ . Thus, for  $L, K = \infty$ , the proposed model satisfies the criteria of the Karhunen-Loève Theorem (Alexanderian, 2015) and spans all possible squared-integrable stochastic processes. Under suitable regularity conditions, similar to Hazra et al. (2018), posterior consistency of the proposed model holds (Wu and Ghosal, 2010; Ghosal and van der Vaart, 2017).

The spatial tail dependence coefficient between two different grid cells  $\mathbf{s}_{n_1}$  and  $\mathbf{s}_{n_2}$ , defined in (1), is nonstationary for the proposed LTP-DPM model and can be shown to be equal to

$$\chi(\mathbf{s}_{n_1}, \mathbf{s}_{n_2}) = 2\overline{F}_T \left( \sqrt{a' \frac{1 - r_m(\mathbf{s}_{n_1}, \mathbf{s}_{n_2})}{1 + r_m(\mathbf{s}_{n_1}, \mathbf{s}_{n_2})}}; 0, 1, a' \right), \quad (9)$$

where  $m = \arg \min_k \{a_k\}$ ,  $a' = a_m + 1$ ,  $r_m(\mathbf{s}_{n_1}, \mathbf{s}_{n_2}) = \mathbf{h}_{n_1} \Phi_m \mathbf{h}'_{n_2} / \sqrt{\prod_{\tilde{n}=n_1, n_2} (\mathbf{h}_{\tilde{n}} \Phi_m \mathbf{h}'_{\tilde{n}} + \tau_m^2)}$  denotes the underlying spatial correlation of the Gaussian term characterizing the  $m$ -th mixture component, and  $\overline{F}_T(\cdot; 0, 1, a) = 1 - F_T(\cdot; 0, 1, a)$  is the survival function for a standard (univariate) Student's  $t$  distribution with  $a$  degrees of freedom. For the derivation of (9), see Hazra et al. (2018). Here,  $\chi(\mathbf{s}_{n_1}, \mathbf{s}_{n_2})$  is nonzero, so our model can capture asymptotic dependence unlike Gaussian processes, and is an increasing function of  $r_m(\mathbf{s}_{n_1}, \mathbf{s}_{n_2})$ . When  $r_m(\mathbf{s}_{n_1}, \mathbf{s}_{n_2}) = 0$ ,  $\chi(\mathbf{s}_{n_1}, \mathbf{s}_{n_2}) = 2\overline{F}(\sqrt{a'}; 0, 1, a') \neq 0$  (unless  $a' \rightarrow \infty$ ). This is a downside of the proposed model in case the spatial domain is large and the climate parameter of interest is rough across the domain (precipitation, for example), but this should not be a big limitation for our Red Sea SST data, which remain strongly dependent at large distances.



## 4 Bayesian inference and identification of hotspots

### 4.1 Hyperpriors and an efficient Gibbs sampler

We draw posterior inference about the model parameters in our model using Markov chain Monte Carlo (MCMC) sampling. Except for the degrees of freedom parameters,  $a_k$ ,  $k = 1, \dots, K$ , of the LTP components of the LTP-DPM model, conjugate priors exist for all other model parameters, which allows Gibbs sampling. While Metropolis–Hastings sampling would be possible for the  $a_k$ ’s, we prefer to consider discrete uniform priors on a fine grid, which allows drawing samples from the full conditional distributions in a fast and easy manner. This strategy is often considered in the literature due to its numerical stability; for example, [Gelfand et al. \(2005\)](#) use it for posterior sampling from the range parameter of the spatial Matérn covariance; see also [Morris et al. \(2017\)](#), [Hazra et al. \(2018\)](#) and [Hazra et al. \(2019\)](#).

For the vectors of fixed effects involved within the mean terms,  $\beta_{i;j}$ ,  $i = 1, 2, j = 1, 2$ , we consider the priors  $\beta_{i;j} \sim \text{Normal}_P(\mu_{i;j}\mathbf{1}_P, \sigma_{i;j}^2\mathbf{I}_P)$ , where  $\mathbf{1}_P$  is the  $P$ -dimensional vector of ones and  $\mathbf{I}_P$  is the  $P$ -by- $P$  identity matrix, with  $P = P_T P_S = 2268$ . While the posterior distribution of  $\beta_{i;j}$  is also a  $P$ -variate normal distribution, we avoid the computationally challenging inversion of the involved high-dimensional posterior covariance matrix through eigen-decomposition. For the hyper-parameters  $\mu_{i;j}$ , we consider the relatively non-informative priors  $\mu_{i;j} \sim \text{Normal}(0, s_{i;j}^2)$  with  $s_{1;j} = 10^2$  and  $s_{2;j} = 10$  for  $j = 1, 2$ . The parameter vectors  $\beta_{1;j}$ ,  $j = 1, 2$ , correspond to the intercept term, while  $\beta_{2;j}$ ,  $j = 1, 2$ , correspond to the slopes. The absolute values of the intercept-related terms are likely to be large while the slope terms, indicators of the rate of change of SST with time, are likely to be close to zero and thus, we consider flatter prior for the  $\mu_{1;j}$ ’s. For the hyper-parameters  $\sigma_{i;j}^2$ , we consider the priors  $\sigma_{i;j}^2 \sim \text{Inverse-Gamma}(a_{i;j}, b_{i;j})$ ,  $i = 1, 2, j = 1, 2$ . We fix the hyper-parameters to  $a_{1;j} = b_{1;j} = 0.01$  and  $a_{2;j} = b_{2;j} = 0.1$  for  $j = 1, 2$ . While both priors are quite non-informative, we choose the hyper-priors differently following a similar logic as the one used when considering the priors for the  $\mu_{i;j}$ ’s.

The parameters involved in the distribution of the error terms  $\varepsilon_t(\mathbf{s}_n)$  are the component-specific parameters and hyper-parameters of the DPM model described in §3.3. For the purpose of computation, we fix the number of components in the stick-breaking prior by setting  $V_K = 1$  for some finite integer  $K$ . The choice of  $K$  is problem-specific, and leads to a bias–variance trade-off. Large  $K$  is desirable to increase the model flexibility (i.e., decrease the bias), but considering  $K$  to be very large may lead to spurious estimates as the sampling from the parameters of a LTP component depend on the observations from that specific cluster and a large  $K$  may lead to very few observations within some clusters (thus increasing the variance). In our application, we fit different models with  $K = 1, 5, 10$  and compare them by cross-validation (see §5.2). The prior choices for the DPM model parameters are  $\Phi_k \stackrel{iid}{\sim}$  Inverse-Wishart( $L + 2, \Delta$ ) where  $\Delta$  is the diagonal containing the  $L$  largest eigenvalues of  $\hat{\Sigma}$  (recall §3.3),  $\tau_k^2 \stackrel{iid}{\sim}$  Inverse-Gamma(1, 1), and  $a_k \stackrel{iid}{\sim}$  Discrete-Uniform(2.1, 2.2,  $\dots$ , 40.0). The prior for  $\Phi_k$  is conjugate and it ensures that  $E(\Phi_k) = \Delta$ . We choose hyper-parameters for the prior of  $\tau_k^2$  so that the mass is mainly distributed near zero. The existence of a continuous conjugate prior for  $a_k$  is unknown and the discrete uniform prior avoids the need of Metropolis–Hastings sampling, as mentioned above. The support of the distribution considered here covers a wide range of degrees of freedom. The smallest values within the support of  $a_k$  correspond to a heavy-tailed and strongly dependent process, while the largest values practically correspond to a near-Gaussian behavior. For the mixing probabilities  $\pi_k$ , we consider a stick-breaking prior as discussed in §3.3. The distribution of  $\boldsymbol{\pi} = [\pi_1, \dots, \pi_K]$  involves the unknown concentration hyper-parameter  $\delta$ . We here consider a fairly non-informative conjugate hyper-prior,  $\delta \sim \text{Gamma}(0.1, 0.1)$ .

The full conditional distributions required for model fitting and prediction are provided in the Supplementary Material. In our data application, we implement the MCMC algorithm in R (<http://www.r-project.org>). We generate 60,000 posterior samples and discard the first 10,000 iterations as burn-in period. Subsequently, we thin the Markov chains by keeping

one out of five consecutive samples and thus, we finally obtain 10,000 samples for drawing posterior inference. Convergence and mixing are monitored through trace plots.

## 4.2 Hotspot estimation

Our main goal is to exploit the observed Red Sea SST data to identify extreme hotspots, i.e., to construct a confidence region that contains joint threshold exceedances of some (very) high threshold  $u$  at some future time  $t_0$  with a predefined probability. Our proposed approach developed below extends [French and Sain \(2013\)](#) (who focus on Gaussian processes) to the more general and flexible case of LTP-DPMs, which better capture the joint tail behavior.

Let  $\mathcal{D}' = \{\mathbf{s}_1, \dots, \mathbf{s}_N\} \subset \mathcal{D}$  be our discretized domain of interest. We define the exceedance region above a threshold  $u$  at time  $t_0$  as  $E_{u+}^0 = \{\mathbf{s} \in \mathcal{D}' \mid Y_{t_0}(\mathbf{s}) \geq u\}$ . Note that because  $Y_{t_0}(\cdot)$  is a random process,  $E_{u+}^0$  is a random set. We want to find a region  $\mathcal{D}_{u+}^0$  so that  $\Pr(E_{u+}^0 \subseteq \mathcal{D}_{u+}^0) = 1 - \alpha$  for some predefined Type I error  $\alpha$ . The approach is akin to multiple hypothesis testing, where we first state a null and an alternative hypothesis and then draw conclusions based on a test statistic and a critical value. The difference is in treating the random process  $Y_{t_0}(\cdot)$  as a “parameter” though the main concept remains same. For each fixed grid cell  $\mathbf{s}_n \in \mathcal{D}'$ , we can individually test the null hypothesis  $H_0 : Y_{t_0}(\mathbf{s}_n) = u$  versus the alternative  $H_1 : Y_{t_0}(\mathbf{s}_n) < u$  based on some test statistic  $\tilde{Y}_{t_0}(\mathbf{s}_n)$ . An obvious choice for  $\tilde{Y}_{t_0}(\mathbf{s}_n)$  is to exploit (a rescaled version of)  $\hat{Y}_{t_0}(\mathbf{s}_n)$ , a predictor of  $Y_{t_0}(\mathbf{s}_n)$ . To find the exceedance region, a possible approach is to combine these single-cell tests by collecting all  $\mathbf{s}_n \in \mathcal{D}'$  where we fail to reject  $H_0$ . To account for multiple testing, we explain below how to set the critical value of the single-cell tests, in order to reach a family-wise error rate  $\alpha$ .

We now first show how to perform single exceedance tests based on our proposed LTP-DPM model (7). We have  $Y_{t_0}(\mathbf{s}_n) = \mu_{t_0}(\mathbf{s}_n) + \varepsilon_{t_0}(\mathbf{s}_n)$ . Let  $t_{01} = \lceil t_0/52 \rceil$  and  $t_{02} = t_0 - 52(t_{01} - 1)$  be the year and week corresponding to  $t_0$ , respectively. The mean of  $Y_{t_0}(\mathbf{s}_n)$  is

$$\mu_{t_0}(\mathbf{s}_n) = \sum_{i=1}^2 \sum_{j=1}^2 x_{t_{01}}^{(0;i)} \left( \mathbf{x}_{t_{02}}^{(1)} \otimes \mathbf{x}_n^{(2;j)} \right) \beta_{i;j}, \quad (10)$$

where  $x_{t_{01}}^{(0;1)} = 1/\sqrt{T_1}$ ,  $x_{t_{01}}^{(0;2)} = \{t_{01} - (1 + T_1)/2\}/\sqrt{\sum_{t_1^*=1}^{T_1}\{t_1^* - (1 + T_1)/2\}^2}$  and  $\mathbf{x}_{t_{02}}^{(1)}$  is the  $t_{02}$ -th row of  $\mathbf{X}_1$ . The density of the corresponding error term  $\varepsilon_{t_0}(\mathbf{s}_n)$  is

$$f(\varepsilon) = \sum_{k=1}^K \pi_k f_T \left\{ \varepsilon; 0, \frac{a_k-2}{a_k} (\mathbf{h}_n \boldsymbol{\Phi}_k \mathbf{h}_n' + \tau_k^2), a_k \right\}, \quad (11)$$

where  $f_T(\cdot; 0, \tilde{\sigma}^2, \tilde{a})$  denotes the density function of a univariate Student's  $t$  distribution with location 0, scale  $\tilde{\sigma}$  and degrees of freedom  $\tilde{a}$ . In the hotspot estimation context,  $Y_{t_0}(\mathbf{s}_n)$  is treated as an unobserved random parameter. Based on the posterior samples from the model parameters (recall §4.1) and the distribution of  $Y_{t_0}(\mathbf{s}_n)$  defined by (10) and (11), we get samples from the posterior predictive distribution of  $Y_{t_0}(\mathbf{s}_n)$ . Let  $\hat{Y}_{t_0}(\mathbf{s}_n)$  be the posterior mean of  $Y_{t_0}(\mathbf{s}_n)$ . From the Bayesian central limit theorem, the large-sample approximation  $\hat{Y}_{t_0}(\mathbf{s}_n) \sim \text{Normal}(Y_{t_0}(\mathbf{s}_n), \sigma_{t_0}(\mathbf{s}_n)/\sqrt{B})$  holds, with  $B = 10000$  the number of samples available from the posterior predictive distribution of  $Y_{t_0}(\mathbf{s}_n)$  and  $\sigma_{t_0}(\mathbf{s}_n)$  the standard deviation of the posterior samples from  $Y_{t_0}(\mathbf{s}_n)$ . This leads to considering the test statistic

$$\tilde{Y}_{t_0}(\mathbf{s}_n) = \frac{\hat{Y}_{t_0}(\mathbf{s}_n) - u}{\tilde{\sigma}_{t_0}(\mathbf{s}_n)}. \quad (12)$$

where  $\tilde{\sigma}_{t_0}(\mathbf{s}_n) = \sigma_{t_0}(\mathbf{s}_n)/\sqrt{B}$ , with a rejection region for  $H_0$  of the form  $\{\tilde{Y}_{t_0}(\mathbf{s}_n) < C_\alpha\}$ . Under the equivalent null hypothesis  $H_0 : Y_{t_0}(\mathbf{s}_n) = u$  (versus  $H_1 : Y_{t_0}(\mathbf{s}_n) < u$ ),  $\tilde{Y}_{t_0}(\mathbf{s}_n)$  has an approximate standard normal distribution.

We now explain how to adjust the critical value  $C_\alpha$ , so that the family-wise Type I error rate is  $\alpha$ . This ensures a confidence level of  $1 - \alpha$  for the confidence region  $\mathcal{D}_{u+}^0$ . A Type I error can only occur at locations  $\mathbf{s}_n$  within the true exceedance region, and hence to control the overall Type I error, we need to consider the test statistic values only within  $E_{u+}^0$ . The critical value  $C_\alpha$  is chosen such that  $\Pr(\min_{\mathbf{s}_n \in E_{u+}^0} \{\tilde{Y}_{t_0}(\mathbf{s}_n)\} < C_\alpha) = \alpha$ . The distribution of  $\min_{\mathbf{s}_n \in E_{u+}^0} \{\tilde{Y}_{t_0}(\mathbf{s}_n)\}$  is unknown but it can be approximated by simulation as follows. For the  $B$  posterior predictive samples  $\{\mathbf{Y}_{t_0}^{(1)}, \dots, \mathbf{Y}_{t_0}^{(B)}\}$  from  $\mathbf{Y}_{t_0} = [Y_{t_0}(\mathbf{s}_1), \dots, Y_{t_0}(\mathbf{s}_N)]'$ , we identify  $E_{u+}^b = \{\mathbf{s}_n \in \mathcal{D}' \mid Y_{t_0}^{(b)}(\mathbf{s}_n) \geq u\}$  for each  $b = 1, \dots, B$ . Subsequently, for each  $\mathbf{s}_n \in E_{u+}^b$ , we calculate  $\tilde{Y}_{t_0}(\mathbf{s}_n)$  and also  $\min_{\mathbf{s}_n \in E_{u+}^b} \{\tilde{Y}_{t_0}(\mathbf{s}_n)\}$ . We repeat this procedure for each

$b$  and estimate  $C_\alpha$  by  $\hat{C}_\alpha$ , the sample  $\alpha$ -th quantile of  $\{\min_{\mathbf{s}_n \in E_{u+}^b} \{\tilde{Y}_{t_0}(\mathbf{s}_n)\}; b = 1, \dots, B\}$ . Finally, the estimated confidence region (i.e., hotspot) is  $\mathcal{D}_{u+}^0 = \{\mathbf{s}_n \in \mathcal{D}' \mid \tilde{Y}_{t_0}(\mathbf{s}_n) \geq \hat{C}_\alpha\}$ .

## 5 Data application

### 5.1 Model fitting and cross-validation study

As discussed in §2, we thin the raw data and keep only one day per week and thus, we obtain 7 “weekly” sub-datasets, analyze them independently and report the averaged results.

To fit our model, we first need to fix the number of mixture components  $K$ , and the number of spatial basis functions (EOFs),  $L$ . Both  $K$  and  $L$  affect the bias-variance trade-off and the computational burden. We specify  $K = 5, 10$ , and  $L = \arg \max_{l \in \{1, \dots, N\}} \{\lambda_l \geq q\lambda_1\}$  with  $q = 0.005, 0.01$ , where  $\lambda_1 > \lambda_2 > \dots, \lambda_N$  are the ordered eigenvalues of  $\hat{\Sigma}$  (recall §3.3). For  $q = 0.01$  and  $q = 0.005$ , we denote the values of  $L$  by  $L_1$  and  $L_2$  respectively. For the Red Sea SST data,  $L_1 = 15$  consistently across all the sub-datasets and  $L_2$  varies between 24 and 26. We then compare the different choices of  $K$  and  $L$  by cross-validation. Moreover, we also compare our proposed LTP-DPM model to some simpler parametric and semiparametric sub-models, namely LGP ( $K = 1, a_k = \infty$ ), LTP ( $K = 1$ ) and LGP-DPM ( $a_k = \infty$ ).

For model comparison, we divide each weekly Red Sea SST sub-dataset into two parts, using the years 1985–2010 (1352 weeks) for training and keeping the years 2011–2015 (260 weeks) for testing. For each spatiotemporal observation in the test set, we estimate the posterior predictive distribution based on the posterior samples and confront the estimated distribution with the test observation. Because our primary goal is to predict high threshold exceedances, we use the Brier score (BS) and the tail-weighted continuous rank probability score (TWCPRPS), proposed by [Gneiting and Raftery \(2007\)](#) and [Gneiting and Ranjan \(2011\)](#), respectively. For a single test sample  $y$ , the BS at a given level  $u$  is defined as  $\text{BS}_u(y, F) = \{\mathbb{I}_{\{y > u\}} - \bar{F}(u)\}^2$ , where  $\bar{F}(\cdot) = 1 - F(\cdot)$  is the survival function corresponding to the posterior predictive distribution  $F$ . For a single test sample  $y$ , the

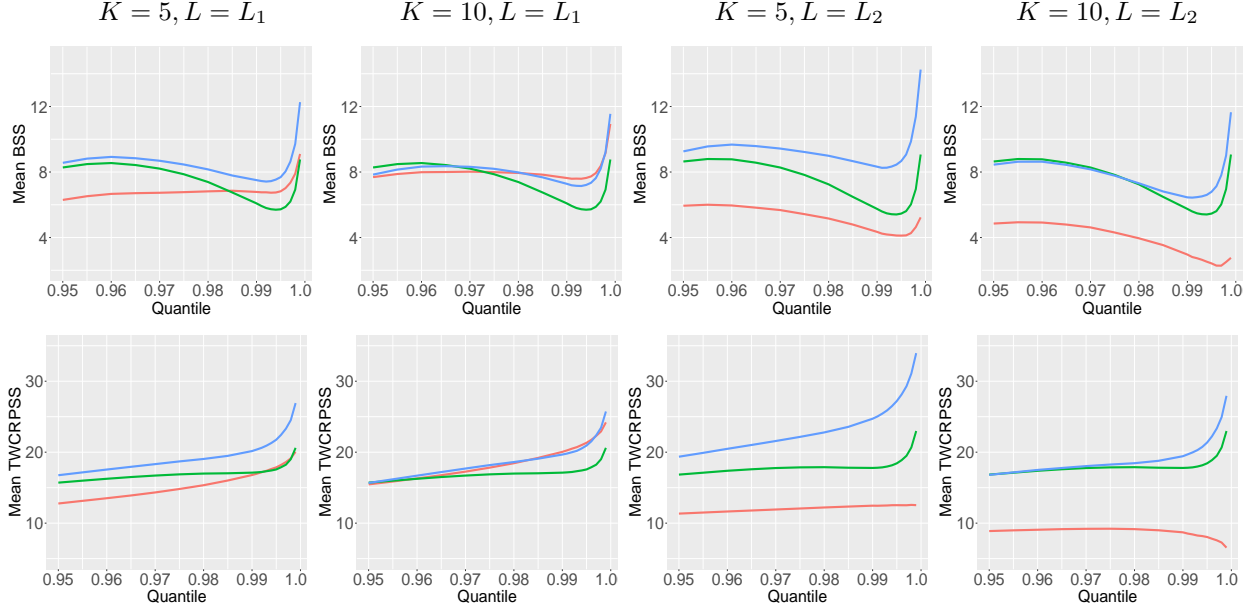


Figure 4: Averaged BSS (top) and TWCPRPS (bottom) for the models LTP (green), LGP-DPM (red) and LTP-DPM (blue) considering the LGP as the reference model, plotted as a function of the threshold  $u$  ranging from the 95%-quantile to the 99.9%-quantile of the observed data. Higher values of BSS and TWCPRPS indicate better prediction performance.

TWCPRPS is defined as  $\text{TWCPRPS}_w(y, F) = \int_{-\infty}^{\infty} w(x) \{F(x) - \mathbb{I}_{\{y \leq x\}}\}^2 dx$ , where  $w(\cdot)$  is a non-negative weight function. To focus on the upper tail, we use  $w(x) = \mathbb{I}_{\{x > u\}}$  so that  $\text{TWCPRPS}_w(y, F) = \int_u^{\infty} \text{BS}_x(y, F) dx$ . Then, we define the Brier skill score (BSS) and tail-weighted continuous rank probability skill score (TWCPRPS) for a model  $M$  as

$$\text{BSS}_M = \frac{\text{BS}_{\text{LGP}} - \text{BS}_M}{\text{BS}_{\text{LGP}}} \times 100\%, \text{TWCPRPS}_M = \frac{\text{TWCPRPS}_{\text{LGP}} - \text{TWCPRPS}_M}{\text{TWCPRPS}_{\text{LGP}}} \times 100\%, \quad (13)$$

using LGP as the benchmark, where  $\text{BS}_M$  and  $\text{TWCPRPS}_M$  are the short-hand notation for the BS and TWCPRPS for a model  $M$ , respectively. When comparing models for a specific  $L$ , we use that same  $L$  for the benchmark. Higher values of BSS or TWCPRPS indicate better prediction performance. We report the results by averaging values over the test set. Figure 4 reports the results plotted as a function of the threshold  $u$ , which ranges between 95% and the 99.9%-quantiles of the SST data. The LGP model is consistently the worst (zero, the benchmark), while our proposed LTP-DPM model is better than the others in most of the cases. Comparing across the choices of  $K$  and  $L$ , the predictive performance is best when

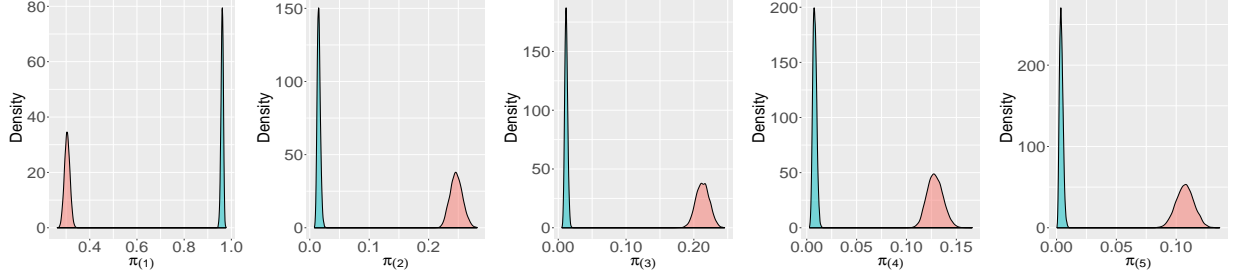


Figure 5: Posterior densities of the five ordered stick-breaking probabilities  $\pi_{(1)} > \dots > \pi_{(K)}$  (left to right), based on fitting the LGP-DPM (pink) and LTP-DPM (blue) models with  $K = 5$  mixture components and  $L = L_2$  spatial basis functions.

$K = 5$  and  $L = L_2$ . Hence, we consider  $K = 5$  and  $L = L_2$  for drawing inferences. Goodness-of-fit diagnostics of the LTP-DPM model are provided in the Supplementary Material.

To explore the DPM models further, we investigate the posterior distribution of stick-breaking probabilities  $\pi_k$ . Because the  $\pi_k$ 's are not identifiable due to label-switching within the MCMC algorithm, Figure 5 displays the estimated densities of the ordered probabilities,  $\pi_{(k)}$ ,  $k = 1, \dots, K$ , for  $K = 5$  and  $L = L_2$ . For the LTP-DPM model, one single cluster fits a large proportion of the temporal replicates, while the remaining four clusters capture the behavior of “abnormal days”, i.e., extreme events. This property is desirable as it allows us to have a separate control over extreme events, being described by different mixture-specific parameters. On the other hand, the LGP-DPM model allocates large probabilities to many clusters. The thin-tailed LGP cluster components fail to allocate the bulk of the distribution into a single cluster for our heavy-tailed SST data. This makes the identification of the bulk and the tail more challenging and requires significantly more clusters for model fitting.

## 5.2 Estimated time trend and return levels

We now discuss the estimated spatial maps of the decadal rate of change (DRC) in mean SST and the return levels (adjusted for non-stationarity) based on our best LTP-DPM model.

We present in Figure 6 the spatial maps of the estimated weekly-varying DRC in mean SST across the Red Sea for Weeks 7 and 34 (the coolest and warmest weeks based on the averaged observed SST, respectively) along with the overall DRC obtained by averaging

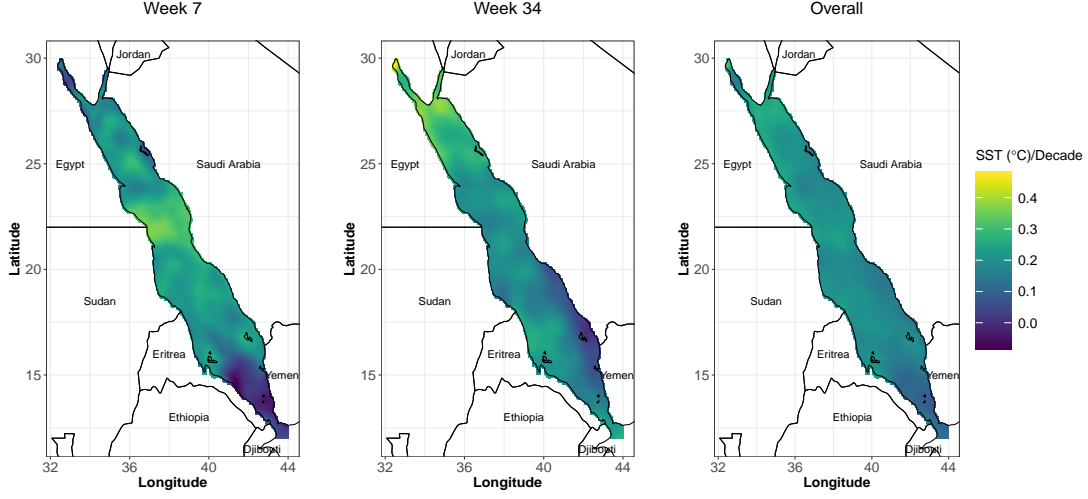


Figure 6: Estimated decadal rate of change in mean SST profile for the coolest (7-th) and the warmest (34-th) weeks along with the estimated overall rate obtained by averaging across the 52 weeks. The sub-figures are on the same scale.

across the 52 weeks. The spatial patterns of DRC for the two weeks are significantly different, which is consistent with the exploratory analysis (Figure 2). For Week 7 (winter), the highest DRC values are near the latitude 22°N while the lowest values are observed near the southern end of the Red Sea. For Week 34 (summer), the highest DRC values are near the northern tip of the Gulf of Suez and over a large coastal region of Egypt as well as the coastal region of northwest Saudi Arabia while the lowest values are observed near the coastal region of the southwest Saudi Arabia. The spatial map of the overall DRC is smoother than the weekly profiles, with higher values being observed near the coastal region of Egypt. In addition, we also calculate the corresponding  $t$ -statistic for each spatial location; see the Supplementary Material. A value of  $|t| > 2$  indicates a (site-wise) significant change at the 95% confidence level in mean SST over the years 1985–2015. While negative estimates of DRC are obtained near the coast of Eritrea for Week 7 (for a total 700 grid cells), all such DRC values are not significant except for 43 grid cells. Similarly, for Week 34, negative estimates of DRC are obtained at 3 grid cells near the coastal region of southwest Saudi Arabia but they are all not significant. Considering the overall DRC, the  $t$ -statistics vary between 8.21 and 36.04 indicating that the overall DRC is positive and significant at all the grid cells.



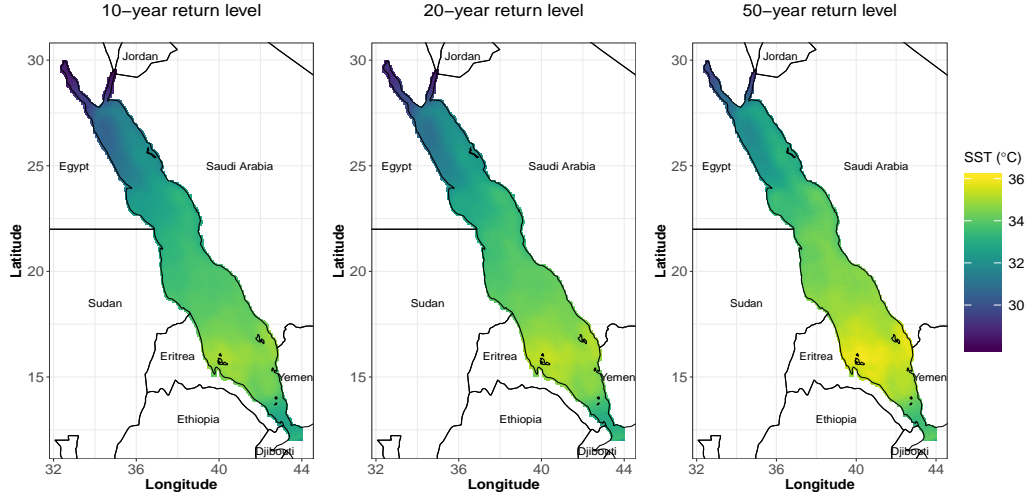


Figure 7: Estimated 10 (left), 20 (middle) and 50 (right)-year return levels for Week 40. All sub-figures share the same scale.

A  $T_0$ -year return level of a stationary weekly time series is the  $(1 - 1/[52T_0])$ -th quantile of its marginal distribution. The LTP-DPM model has a nonstationary mean and involves both trend and seasonality. Thus, quantiles—hence return levels—change over time. As the model involves a linear trend for each week, we follow [Cheng et al. \(2014\)](#) and consider the mid-year of the return period as the effective year, and calculate the mean SST accordingly. Here, we concentrate specifically on some of the warmest weeks. While the spatial average SST is maximum for Week 34, Week 40 is hottest week for 2860 grid cells spread between Eritrea and southwest Saudi Arabia, which covers some major coral reefs. The results for Weeks 33 and 34 are discussed in the Supplementary Material. For the Week 40, Figure 7 provides the spatial maps of 10-year, 20-year and 50-year estimated return levels considering 2020 as the reference year. For all three return periods, low estimates are obtained near the Gulf of Suez and the Gulf of Aqaba and high estimates are observed across a large region between the coast of Eritrea and the southwest of Saudi Arabia. The three return level profiles exceed  $35^\circ\text{C}$ , the coral bleaching threshold according to [Jokiel and Brown \(2004\)](#), at 60, 1313 and 4285 grid cells, respectively. This suggests that very extreme sea temperatures (potentially causing intense coral bleaching) might occur over the next century.

### 5.3 Estimated joint exceedance probabilities

We now investigate model-based joint exceedance probabilities in more detail, and consider three specific regions: the Dahlak Islands of Eritrea (40.13°E, 15.77°N), the Farasan Islands of Saudi Arabia (41.88°E, 16.82°N), and the region of Thuwal in Saudi Arabia (38.88°E, 22.37°N), where large coral reefs are present. Projecting to the year 2100, we estimate two types of exceedance probabilities, namely  $\Pr(\cup_{\mathbf{s}_n \in \mathcal{D}_0} \{Y_{t_0}(\mathbf{s}_n) > u\})$  and  $\Pr(\cap_{\mathbf{s}_n \in \mathcal{D}_0} \{Y_{t_0}(\mathbf{s}_n) > u\})$ , for a range of high temperature values  $u$  and different neighborhoods  $\mathcal{D}_0$ , i.e., sets of grid cells within a certain distance from the three specific locations. For  $\mathcal{D}_0$ , we consider distances 0 km (i.e., the marginal case, where both the types of probabilities coincide), 6 km (including the first order neighbors), 10 km, 20 km, 30 km and 50 km. A large value of  $\Pr(\cup_{\mathbf{s}_n \in \mathcal{D}_0} \{Y_{t_0}(\mathbf{s}_n) > u\})$  indicates a high probability that *at least one* grid cell within  $\mathcal{D}_0$  exceeds the threshold  $u$ , so it represents the risk of partial coral bleaching within the region. A large value of  $\Pr(\cap_{\mathbf{s}_n \in \mathcal{D}_0} \{Y_{t_0}(\mathbf{s}_n) > u\})$  indicates a high probability that *all* grid cells within  $\mathcal{D}_0$  exceed the threshold  $u$ , so it represents the risk of a mass coral bleaching. These probabilities are different across weeks. The results for Weeks 33 and 34 are provided in the Supplementary Material. For Week 40, the values are presented in the top panel of Figure 8. For Dahlak Islands of Eritrea and Farasan Islands of Saudi Arabia, the exceedance probabilities are high even for high thresholds. As Week 40 is a post-summer week in the northern Red Sea, the exceedance probabilities are comparatively lower for Thuwal, Saudi Arabia. At a threshold of 35°C, the estimated probability values (combining both types of exceedance probabilities) range within (0.0130, 0.4665), (0.0086, 0.5208) and (0.0003, 0.0227) for the three regions, respectively. These values indicate high risk of coral bleaching at least partially near the first two regions.

While Jokieli and Brown (2004) consider a coral bleaching threshold of 35°C for the Gulf Region, Genevieve et al. (2019) discuss spatially-varying thresholds across the Red Sea mentioning that warmer regions have higher bleaching thresholds, while cooler region have lower

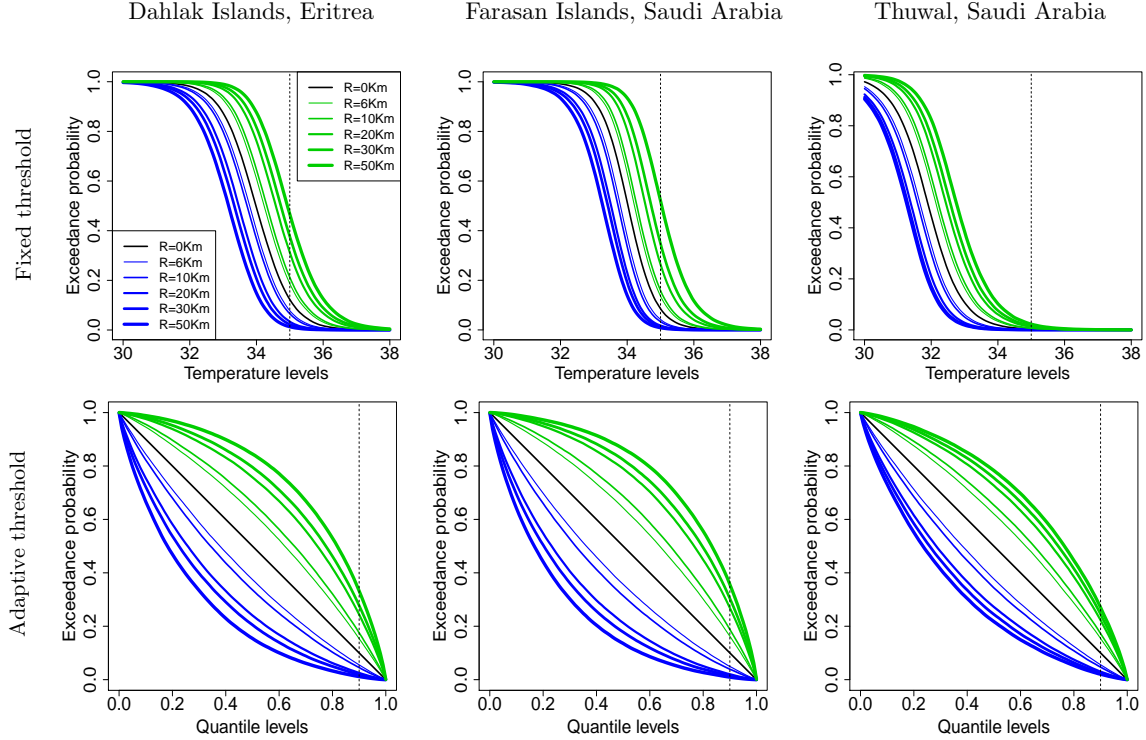


Figure 8: Exceedance probabilities of SST across all the grid cells (blue) or at least one grid cell (green) within 0 km (the marginal case), 6 km (including the first order neighbors), 10 km, 20 km, 30 km and 50 km distances from (40.13°E, 15.77°N) near Dahlak Islands of Eritrea, (41.88°E, 16.82°N) near Farasan Islands of Saudi Arabia and (38.88°E, 22.37°N) near Thuwal of Saudi Arabia at different temperature levels for Week 40 of the reference year 2100 considering fixed bleaching threshold theory (top) and the exceedance probabilities for different marginal quantile levels considering adaptive bleaching threshold theory (bottom).

bleaching thresholds. [Logan et al. \(2014\)](#) discusses the adaptive nature of coral reefs for moderate climate changes. Considering these theories, we re-estimate the two types of exceedance probabilities, but instead of calculating them over a range of spatially-constant temperature levels, here we calculate them for different site-specific marginal quantiles. While the coral reefs are assumed to be adaptive to the mean temperature level, an extreme positive deviation (exceeding 90%-quantiles, for example) could be a possible reason for coral bleaching. For any  $p \in (0, 1)$ , let  $Q_{t_0}^{(n)}(p)$  be the  $p$ -th quantile function of the distribution of  $Y_{t_0}(\mathbf{s}_n)$  at the  $n$ -th grid cell,  $\mathbf{s}_n$ , for the reference time  $t_0$ . We estimate the probabilities  $\Pr\left(\bigcup_{\mathbf{s}_n \in \mathcal{D}_0} \{Y_{t_0}(\mathbf{s}_n) > Q_{t_0}^{(n)}(p)\}\right)$  and  $\Pr\left(\bigcap_{\mathbf{s}_n \in \mathcal{D}_0} \{Y_{t_0}(\mathbf{s}_n) > Q_{t_0}^{(n)}(p)\}\right)$  for the same

choices of  $\mathcal{D}_0$  as above. Let  $Q^{(n)}(p)$  be the  $p$ -th quantile function of the (temporally invariant) distribution of  $\varepsilon_{t_0}(\mathbf{s}_n)$ . Following (2), we have  $Q_{t_0}^{(n)}(p) = \mu_{t_0}(\mathbf{s}_n) + Q^{(n)}(p)$ , so  $\Pr\left(\cup_{\mathbf{s}_n \in \mathcal{D}_0} \{Y_{t_0}(\mathbf{s}_n) > Q_{t_0}^{(n)}(p)\}\right) = \Pr\left(\cup_{\mathbf{s}_n \in \mathcal{D}_0} \{\varepsilon_{t_0}(\mathbf{s}_n) > Q^{(n)}(p)\}\right)$ , which does not change over time. Similarly,  $\Pr\left(\cap_{\mathbf{s}_n \in \mathcal{D}_0} \{Y_{t_0}(\mathbf{s}_n) > Q_{t_0}^{(n)}(p)\}\right) = \Pr\left(\cap_{\mathbf{s}_n \in \mathcal{D}_0} \{\varepsilon_{t_0}(\mathbf{s}_n) > Q^{(n)}(p)\}\right)$ . For low through high values of  $p$ , we present the two types of exceedance probabilities in the bottom panel of Figure 8. At a marginal quantile level of 0.9, the estimated probabilities range within (0.0118, 0.3323), (0.0097, 0.3567) and (0.0205, 0.2704) for the three regions, respectively. These values indicate again a high risk of coral bleaching at least in some regions even if the corals are adaptive to local temperature level.

## 5.4 Estimated hotspots

After exploring the joint threshold exceedance probabilities for fixed regions, we now focus on identifying the regions at risk themselves, i.e., hotspots. Projecting to the year 2100, we estimate the 95% confidence regions  $\mathcal{D}_{u+}^0$  for joint exceedance levels  $u = 33^\circ\text{C}$ ,  $u = 33.5^\circ\text{C}$  and  $u = 34^\circ\text{C}$ . The spatial maps of  $\mathcal{D}_{u+}^0$  for Weeks 34 and 40 are presented in Figure 9. The results for other summer weeks are provided in the Supplementary Material.

For Week 34 and  $u = 33^\circ\text{C}$ , the exceedance region covers the entire coast of Eritrea along with the coral reefs of the Dahlak Islands and also some small regions in the middle and the northern parts of the Red Sea. For  $u = 33.5^\circ\text{C}$ , the estimated  $\mathcal{D}_{u+}^0$  covers most of the coast of Eritrea, Dahlak Islands and a tiny region in the mid-Red Sea. For  $u = 34^\circ\text{C}$ , the estimated  $\mathcal{D}_{u+}^0$  still covers a large portion near the coast of Eritrea and also Dahlak Islands. The total number of grid cells within  $\mathcal{D}_{u+}^0$  is 4847, 2555 and 1230 in these three cases, respectively.

For Week 40,  $\mathcal{D}_{u+}^0$  stretches over a major portion of the southern Red Sea for each temperature threshold considered. For  $u = 33^\circ\text{C}$ , the estimated  $\mathcal{D}_{u+}^0$  covers almost entirely the area within the latitudes  $13.5^\circ\text{N}$  and  $19^\circ\text{N}$  and also a small region near coastal Djibouti. For  $u = 33.5^\circ\text{C}$ , the estimated  $\mathcal{D}_{u+}^0$  covers a large region between the latitudes  $14^\circ\text{N}$  and  $18^\circ\text{N}$ .

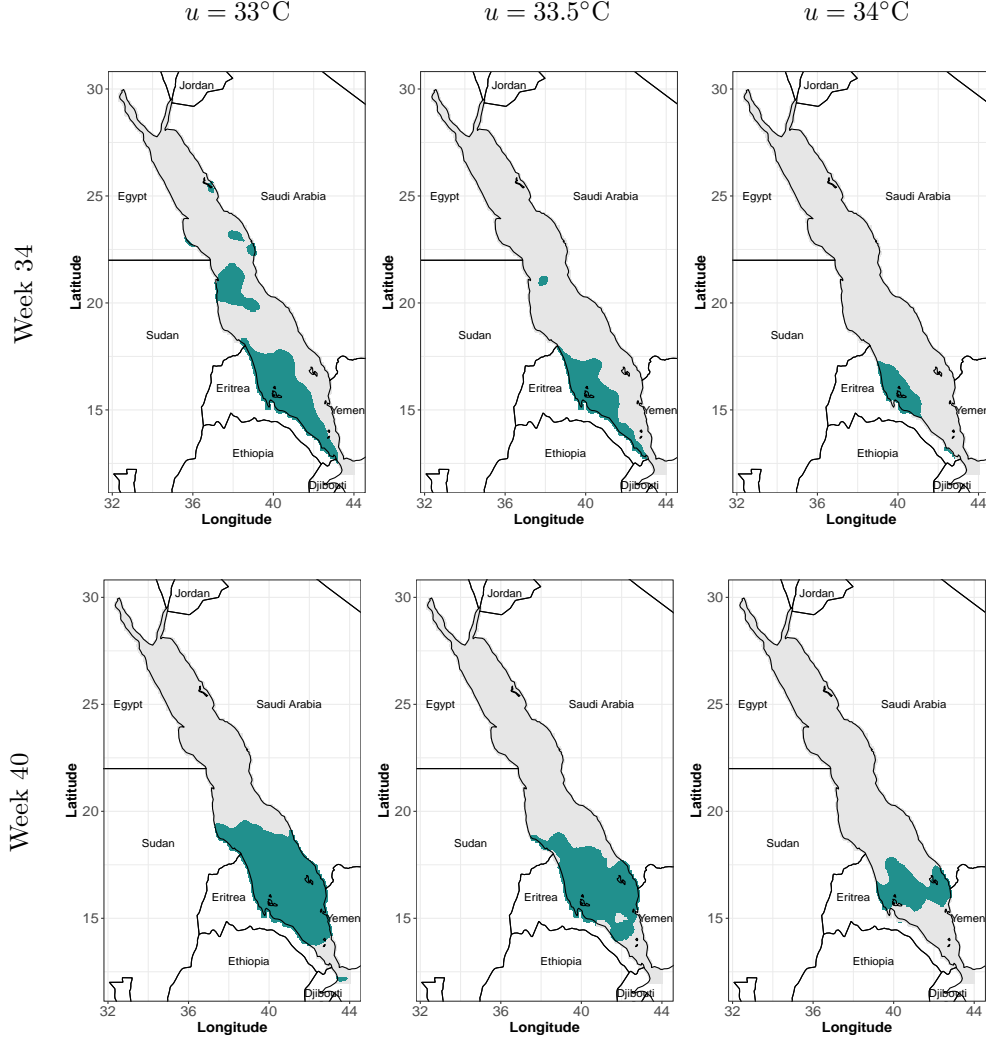


Figure 9: The 95% confidence regions  $\mathcal{D}_{u+}^0$  of the Red Sea SST profile, projected to year 2100, for exceedance levels  $u = 33^\circ\text{C}$ ,  $u = 33.5^\circ\text{C}$  and  $u = 34^\circ\text{C}$  for Weeks 33 and 40.

Finally, for  $u = 34^\circ\text{C}$ , the estimated  $\mathcal{D}_{u+}^0$  covers a region stretched between the latitudes  $15.5^\circ\text{N}$  and  $17.5^\circ\text{N}$  covering the coral reefs of the Dahlak Islands of Eritrea and Farasan Islands of Saudi Arabia. The total number of grid cells within  $\mathcal{D}_{u+}^0$  are 6813, 5044 and 2167 in these three cases, respectively.

## 6 Discussion and perspectives

In this paper, we have proposed a novel low-rank semiparametric Bayesian spatial model for high-dimesnional spatiotemporal data with spatial tail-dependence, where the observa-

tions are assumed to be independent across time. The proposed model has a flexible mean structure that captures trend, seasonality and spatial variability in the mean component. Using B-splines for modeling seasonality and spatial variability help identifying local spatiotemporal features. Relaxing the parametric Gaussian process (GP) assumption that is generally used in the analysis of high-dimensional spatial data, we propose a semiparametric model that captures the variability more flexibly and also the covariance structure of the proposed model provides a good sparse approximation to the highly nonstationary sample spatial covariance. While a finite Dirichlet process mixture of GPs relaxes the parametric GP assumption, it is not apt for modeling data where spatial extremal dependence is present and we circumvent this issue through a mixture of spatial Student's  $t$  processes. We have also developed a hotspot estimation method tailored for our proposed model, which allows us to identify regions at risk of joint extreme events.

Our statistical analysis revealed several important features of the Red Sea SST data. The decadal rate of change in mean SST varies spatially as well as seasonally; while the mean SST is generally lower in the northern Red Sea compared to other regions during summer, its increasing rate is higher in the northern Red Sea compared to the southern parts. We also discussed long-term return levels for some hot weeks that explain the chances of very high temperatures in the near future mainly in the southern Red Sea. Moreover, we calculated two types of exceedance probabilities for three regions of the Red Sea where large coral reefs are present, considering a general coral bleaching cutoff theory as well as the spatially-varying bleaching threshold theory, which takes the adaptive nature of the corals into account. High estimates of these probabilities indicate significant chances of (at least) partial coral bleaching near Dahlak Islands of Eritrea and Farasan Islands. Our estimation of hotspots (i.e., 95% credible region for joint high threshold exceedances) is useful to identify regions with high risk of coral bleaching. Our estimated hotspots cover large coral reefs in the southern Red Sea from an environmental and ecological perspective.

While the proposed model is able to capture several features of the data very flexibly, it has a few downsides. First, the model assumes that the temporal replicates are independent in time, which may not be realistic with daily or sub-daily data. The spatiotemporal model of [Hazra et al. \(2018\)](#), which assumes a copula structure in time, is a possible solution to this issue, but it is limited to small spatiotemporal datasets. No closed form expression of the full posterior exists for the random effects involved in that model and hence the analysis becomes computationally challenging for large temporal dimensions. The MCMC based on deterministic transformations proposed by [Dutta and Bhattacharya \(2014\)](#) could be a possible computationally feasible solution. Additionally, the model of [Hazra et al. \(2018\)](#) assumes that the temporal dependence structure is spatially-invariant which is not a realistic assumption for a large geographic region like the Red Sea. Finally, the spatial extremal dependence is nonzero throughout the spatial domain in our proposed model. The spatial partitioning approach of [Morris et al. \(2017\)](#) could be a possible solution to this issue.

## References

- Alexanderian, A. (2015). A brief note on the Karhunen-Loève expansion. *arXiv preprint arXiv:1509.07526*.
- Anderes, E., Huser, R., Nychka, D., and Coram, M. (2013). Nonstationary positive definite tapering on the plane. *Journal of Computational and Graphical Statistics*, 22(4):848–865.
- Banerjee, S., Gelfand, A. E., Finley, A. O., and Sang, H. (2008). Gaussian predictive process models for large spatial data sets. *Journal of the Royal Statistical Society: Series B (Statistical Methodology)*, 70(4):825–848.
- Beaky, M. M., Scherrer, R. J., and Villumsen, J. V. (1992). Topology of large-scale structure in seeded hot dark matter models. *The Astrophysical Journal*, 387:443–448.
- Berumen, M. L., Hoey, A. S., Bass, W. H., Bouwmeester, J., Catania, D., Cochran, J. E., Khalil, M. T., Miyake, S., Mughal, M., Spaet, J. L., et al. (2013). The status of coral reef ecology research in the Red Sea. *Coral Reefs*, 32(3):737–748.
- Bolin, D. and Lindgren, F. (2015). Excursion and contour uncertainty regions for latent Gaussian models. *Journal of the Royal Statistical Society: Series B (Statistical Methodology)*, 77(1):85–106.

- Bopp, G., Shaby, B. A., and Huser, R. (2019a). A hierarchical max-infinitely divisible process for extreme areal precipitation over watersheds. *arXiv preprint 1805.06084*.
- Bopp, G. P., Shaby, B. A., Forest, C. E., and Mejía, A. (2019b). Projecting flood-inducing precipitation with a bayesian analogue model. *arXiv preprint arXiv:1911.05881*.
- Castruccio, S., Huser, R., and Genton, M. G. (2016). High-order Composite Likelihood Inference for Max-Stable Distributions and Processes. *Journal of Computational and Graphical Statistics*. To appear.
- Cheng, L., AghaKouchak, A., Gilleland, E., and Katz, R. W. (2014). Non-stationary extreme value analysis in a changing climate. *Climatic change*, 127(2):353–369.
- Cooley, D. and Sain, S. R. (2010). Spatial hierarchical modeling of precipitation extremes from a regional climate model. *Journal of agricultural, biological, and environmental statistics*, 15(3):381–402.
- Craigmile, P. F., Cressie, N. A. C., Santner, T. J., and Rao, Y. (2006). A loss function approach to identifying environmental exceedances. *Extremes*, 8:143–159.
- Cressie, N. A. C., Zhang, J., and Craigmile, P. F. (2005). Geostatistical prediction of spatial extremes and their extent. In Renard, P., Demougeot-Renard, H., and Froidevaux, R., editors, *Geostatistics for Environmental Applications, Proceedings of the Fifth Conference on Geostatistics for Environmental Applications*, pages 27–37, Berlin. Springer.
- Davison, A. C. and Huser, R. (2015). Statistics of extremes. *Annual Review of Statistics and its Application*, 2:203–235.
- Davison, A. C., Huser, R., and Thibaud, E. (2013). Geostatistics of dependent and asymptotically independent extremes. *Mathematical Geosciences*, 45(5):511–529.
- Davison, A. C., Huser, R., and Thibaud, E. (2019). Spatial Extremes. In Gelfand, A. E., Fuentes, M., Hoeting, J. A., and Smith, R. L., editors, *Handbook of Environmental and Ecological Statistics*, pages 711–744. CRC Press.
- Davison, A. C., Padoan, S. A., and Ribatet, M. (2012). Statistical modeling of spatial extremes. *Statistical Science*, 27(2):161–186.
- de Fondeville, R. and Davison, A. C. (2018). High-dimensional peaks-over-threshold inference. *Biometrika*, 105(3):575–592.
- Donlon, C. J., Martin, M., Stark, J., Roberts-Jones, J., Fiedler, E., and Wimmer, W. (2012). The operational sea surface temperature and sea ice analysis (OSTIA) system. *Remote Sensing of Environment*, 116:140–158.



- Duan, J. A., Guindani, M., and Gelfand, A. E. (2007). Generalized spatial Dirichlet process models. *Biometrika*, 94(4):809–825.
- Dutta, S. and Bhattacharya, S. (2014). Markov chain Monte Carlo based on deterministic transformations. *Statistical Methodology*, 16:100–116.
- Eklundh, L. and Olsson, L. (2003). Vegetation index trends for the African Sahel 1982–1999. *Geophysical Research Letters*, 30(8).
- French, J. P. and Sain, S. R. (2013). Spatio-temporal exceedance locations and confidence regions. *The Annals of Applied Statistics*, 7(3):1421–1449.
- Fuentes, M. (2007). Approximate likelihood for large irregularly spaced spatial data. *Journal of the American Statistical Association*, 102(477):321–331.
- Furrer, R., Genton, M. G., and Nychka, D. (2006). Covariance tapering for interpolation of large spatial datasets. *Journal of Computational and Graphical Statistics*, 15(3):502–523.
- Furrer, R., Knutti, R., Sain, S., Nychka, D., and Meehl, G. (2007). Spatial patterns of probabilistic temperature change projections from a multivariate Bayesian analysis. *Geophysical Research Letters*, 34(6).
- Gelfand, A. E., Kottas, A., and MacEachern, S. N. (2005). Bayesian nonparametric spatial modeling with Dirichlet process mixing. *Journal of the American Statistical Association*, 100(471):1021–1035.
- Gelfand, A. E. and Schliep, E. M. (2016). Spatial statistics and Gaussian processes: A beautiful marriage. *Spatial Statistics*, 18:86–104.
- Genevier, L. G., Jamil, T., Raitsos, D. E., Krokos, G., and Hoteit, I. (2019). Marine heatwaves reveal coral reef zones susceptible to bleaching in the red sea. *Global change biology*.
- Ghosal, S. and van der Vaart, A. (2017). *Fundamentals of nonparametric Bayesian inference*, volume 44. Cambridge University Press.
- Gneiting, T. and Raftery, A. E. (2007). Strictly proper scoring rules, prediction, and estimation. *Journal of the American Statistical Association*, 102(477):359–378.
- Gneiting, T. and Ranjan, R. (2011). Comparing density forecasts using threshold-and quantile-weighted scoring rules. *Journal of Business & Economic Statistics*, 29(3):411–422.
- Hazra, A., Reich, B. J., Shaby, B. A., and Staicu, A.-M. (2018). A semiparametric Bayesian model for spatiotemporal extremes. *arXiv preprint arXiv:1812.11699*.

- Hazra, A., Reich, B. J., and Staicu, A.-M. (2019). A multivariate spatial skew- $t$  process for joint modeling of extreme precipitation indexes. *Environmetrics*, pages 1–19.
- Higdon, D. (2002). Space and space-time modeling using process convolutions. In *Quantitative methods for current environmental issues*, pages 37–56. Springer.
- Huser, R., Dombry, C., Ribatet, M., and Genton, M. G. (2019). Full likelihood inference for max-stable data. *Stat*, 8:e218.
- Huser, R., Opitz, T., and Thibaud, E. (2017). Bridging asymptotic independence and dependence in spatial extremes using Gaussian scale mixtures. *Spatial Statistics*, 21:166–186.
- Huser, R. and Wadsworth, J. L. (2019). Modeling spatial processes with unknown extremal dependence class. *Journal of the American Statistical Association*, 114(525):434–444.
- Jokiel, P. L. and Brown, E. K. (2004). Global warming, regional trends and inshore environmental conditions influence coral bleaching in hawaii. *Global Change Biology*, 10(10):1627–1641.
- Krishnan, P., Dam Roy, S., George, G., Srivastava, R., Anand, A., Murugesan, S., Kaliyamoorthy, M., Vikas, N., and Soundararajan, R. (2011). Elevated sea surface temperature during May 2010 induces mass bleaching of corals in the Andaman. *Current Science*, 100(1):111–117.
- Lewandowska, A. M., Boyce, D. G., Hofmann, M., Matthiessen, B., Sommer, U., and Worm, B. (2014). Effects of sea surface warming on marine plankton. *Ecology letters*, 17(5):614–623.
- Logan, C. A., Dunne, J. P., Eakin, C. M., and Donner, S. D. (2014). Incorporating adaptive responses into future projections of coral bleaching. *Global Change Biology*, 20(1):125–139.
- Mejia, A. F., Yue, Y., Bolin, D., Lindgren, F., and Lindquist, M. A. (2019). A Bayesian general linear modeling approach to cortical surface fMRI data analysis. *Journal of the American Statistical Association*, pages 1–26.
- Morris, S. A., Reich, B. J., Thibaud, E., and Cooley, D. (2017). A space-time skew- $t$  model for threshold exceedances. *Biometrics*, 73(3):749–758.
- Opitz, T. (2013). Extremal  $t$ -processes: Elliptical domain of attraction and a spectral representation. *Journal of Multivariate Analysis*, 122:409–413.
- Opitz, T., Huser, R., Bakka, H., and Rue, H. (2018). INLA goes extreme: Bayesian tail regression for the estimation of high spatio-temporal quantiles. *Extremes*, 21(3):441–462.
- Padoan, S. A., Ribatet, M., and Sisson, S. A. (2010). Likelihood-based inference for max-stable processes. *Journal of the American Statistical Association*, 105(489):263–277.

- Reaser, J. K., Pomerance, R., and Thomas, P. O. (2000). Coral bleaching and global climate change: scientific findings and policy recommendations. *Conservation biology*, 14(5):1500–1511.
- Reich, B. J. and Shaby, B. A. (2012). A hierarchical max-stable spatial model for extreme precipitation. *The Annals of Applied Statistics*, 6(4):1430.
- Rue, H. and Held, L. (2005). *Gaussian Markov random fields: theory and applications*. Chapman and Hall/CRC.
- Rue, H., Martino, S., and Chopin, N. (2009). Approximate Bayesian inference for latent Gaussian models by using integrated nested Laplace approximations. *Journal of the Royal Statistical Society: Series B (Statistical Methodology)*, 71(2):319–392.
- Sang, H. and Gelfand, A. E. (2009). Hierarchical modeling for extreme values observed over space and time. *Environmental and Ecological Statistics*, 16(3):407–426.
- Sang, H. and Gelfand, A. E. (2010). Continuous spatial process models for spatial extreme values. *Journal of Agricultural, Biological, and Environmental Statistics*, 15(1):49–65.
- Sethuraman, J. (1994). A constructive definition of Dirichlet priors. *Statistica Sinica*, pages 639–650.
- Smith, R. L. (1990). Max-stable processes and spatial extremes. *Unpublished manuscript*.
- Stein, M. (1999). *Statistical Interpolation of Spatial Data*. Springer, New York.
- Stein, M. L., Chi, Z., and Welty, L. J. (2004). Approximating likelihoods for large spatial data sets. *Journal of the Royal Statistical Society: Series B (Statistical Methodology)*, 66(2):275–296.
- Thibaud, E. and Opitz, T. (2015). Efficient inference and simulation for elliptical Pareto processes. *Biometrika*, 102(4):855–870.
- Vecchia, A. V. (1988). Estimation and model identification for continuous spatial processes. *Journal of the Royal Statistical Society: Series B (Methodological)*, 50(2):297–312.
- Wikle, C. K. (2010). Low-rank representations for spatial processes. In *Handbook of spatial statistics*, pages 114–125. CRC Press.
- Wikle, C. K. and Cressie, N. (1999). A dimension-reduced approach to space-time Kalman filtering. *Biometrika*, 86(4):815–829.
- Wu, Y. and Ghosal, S. (2010). The  $L_1$ -consistency of Dirichlet mixtures in multivariate Bayesian density estimation. *Journal of Multivariate Analysis*, 101(10):2411–2419.